Materials Advances

ROYAL SOCIETY OF CHEMISTRY

PAPER

View Article Online
View Journal | View Issue

Check for updates

Cite this: *Mater. Adv.*, 2024, 5, 7349

Comprehensive investigation of multifunctional polyaniline/reduced graphene oxide nanocomposites synthesized from deep eutectic solvents: experimental, RSM, ANN and computational studies†

Abir Boublia, ‡[a] Zahir Guezzout,[b] Nacerddine Haddaoui,[a] Michael Badawi,[c] Imane Lakikza,[d] Ilyas Belkhettab,[e] Ouahiba Moumeni,[f] Saoussen Imene Aouni,[d] Manawwer Alam[g] and Yacine Benguerba*[h]

This work reports a comprehensive investigation into the synthesis, modeling, and characterization of multifunctional polyaniline/reduced graphene oxide (PANI/rGO) nanocomposites, with a focus on their synthesis using deep eutectic solvents (DES). Leveraging an *in situ* chemical polymerization method, PANI/rGO nanocomposites were successfully synthesized, introducing a novel approach employing DES as the electrolyte. The study utilized response surface methodology (RSM), artificial neural networks (ANN), and molecular simulation techniques to model, optimize, and characterize the nanocomposites comprehensively. RSM analysis disclosed the impact of APS/ANI molar ratio, rGO loading, and polymerization time on electrical conductivity, with optimal conditions identified: APS/ANI molar ratio of 0.75, 3 wt% rGO loading, and a 6-hour polymerization time, yielding a high electrical conductivity of 4.975×10^{-3} S cm^{-1}. Integration of ANN techniques enhanced predictive accuracy, reaching an electrical conductivity of 4.988×10^{-3} S cm^{-1}, surpassing RSM. Characterization techniques including UV-vis, PL, Raman, FTIR, and XRD highlighted structural changes, while XPS analysis revealed intensified C–N peaks in PANI/rGO, indicating a denser nanocomposite coating. Electrochemical studies showcased superior capacitance at 145.79 F g^{-1}, surpassing individual components, and TGA analysis revealed enhanced thermal stability. Molecular-level insights provided a nuanced understanding of the PANI–rGO system through FMO, COSMO-RS, NCI, and QTAIM analyses. The study not only presents an innovative synthesis method but also positions PANI/rGO nanocomposites as promising materials for supercapacitors and gas sensors, offering potential for advancements in green chemistry and eco-friendly innovations.

Received 8th March 2024,
Accepted 21st August 2024

DOI: 10.1039/d4ma00231h

rsc.li/materials-advances

Open Access Article. Published on 22 August 2024. Downloaded on 7/19/2025 1:42:39 AM.
This article is licensed under a Creative Commons Attribution-NonCommercial 3.0 Unported Licence.

[a] *Laboratoire de Physico-Chimie des Hauts Polymères (LPCHP), Département de Génie des Procédés, Faculté de Technologie, Université Ferhat ABBAS Sétif-1, 19000, Sétif, Algeria. E-mail: abir.boublia@univ-setif.dz, n_haddaoui@yahoo.com*
[b] *Unité de Recherche sur les Matériaux Emergents –Sétif- URMES, Equipe de Valorisation Des Polymères, Université Ferhat ABBAS Sétif-1, 19000, Sétif, Algeria. E-mail: z.guezzout@univ-setif.dz*
[c] *Université de Lorraine, CNRS, L2CM, F-57000 Metz, France. E-mail: michael.badawi@univ-lorraine.fr*
[d] *Laboratory of physics for matter and radiation, Mohamed Cherif Messadia-souk Ahras University, PO Box 1553, SoukAhras 41000, Algeria. E-mail: lakikza.imane96@gmail.com, sawsenaouni18@gmail.com*
[e] *Laboratory of Electrochemistry-Corrosion, Metallurgy and Inorganic Chemistry, Faculty of Chemistry, USTHB, BP 32 El-Alia, 16111 Algiers, Algeria. E-mail: ilyasbelkhettab@gmail.com*
[f] *Laboratoire d'Electrochimie des Matériaux Moléculaires et Complexes (LEMMC), Département de Génie des Procédés, Faculté de Technologie, Université Ferhat Abbas Setif-1, El-Maabouda, 19000, Sétif, Algeria. E-mail: ouahibamoumeni_wah@yahoo.fr*
[g] *Department of Chemistry, College of Science, King Saud University, PO Box 2455, Riyadh 11451, Saudi Arabia. E-mail: maalam@ksu.edu.sa*
[h] *Laboratoire de Biopharmacie Et Pharmacotechnie (LPBT), Ferhat Abbas Sétif 1 University, 19000, Sétif, Algeria. E-mail: yacinebenguerba@univ-setif.dz*

† Electronic supplementary information (ESI) available. See DOI: https://doi.org/10.1039/d4ma00231h

‡ First authorship: Abir Boublia.

© 2024 The Author(s). Published by the Royal Society of Chemistry

Open Access Article. Published on 22 August 2024. Downloaded on 7/19/2025 1:42:39 AM. This article is licensed under a Creative Commons Attribution-NonCommercial 3.0 Unported Licence.

1. Introduction

Polyaniline (PANI) has been a subject of extensive investigation due to its noteworthy characteristics, drawing significant interest for possible use in electronic devices such as batteries, capacitors, and sensor materials. Its outstanding conductivity and adaptable features position it as a compelling choice for advancing modern electronic technologies.[1–3] Notably, the combination of PANI with carbonaceous elements in nanocomposites has surfaced as an attractive tactic for crafting sophisticated materials, capitalizing on their mutually beneficial attributes. PANI is distinguished by its outstanding electrical conductivity, elevated pseudocapacitance, and robust resilience against environmental degradation.[4,5] Simultaneously, carbonaceous materials, encompassing graphene, carbon nanotubes, and carbon black, are recognized for their remarkable mechanical strength, extensive surface area, and excellent electrical conductivity. Researchers have significantly enhanced electrochemical performance through this combination, making these materials well-suited for diverse applications.[6,7] Among carbon-based materials, graphene distinguishes itself with exceptional electrical, thermal, and mechanical characteristics.[8,9] Its low density,[10] remarkable specific surface area,[11] and robust electron mobility[12] position it as an ideal substrate for embedding active polymers in nanocomposites.[13] Since its groundbreaking discovery in 2004 by Geim and Novoselov,[14] researchers have extensively investigated the integration of graphene as a nanofiller into PANI for the development of versatile nanocomposites. The synergistic interplay between these components has resulted in significant enhancements in their thermal, electrical, mechanical, optical, and electrochemical properties when compared to either pristine PANI or standalone graphene.[13,15] Nevertheless, graphene faces challenges like insolubility in aqueous environments and a tendency to agglomerate due to van der Waals interactions between its sheets. In response to these challenges, derivatives of graphene, particularly reduced graphene oxide (rGO), have emerged as promising nanofillers for polymer nanocomposites.[16–18] Extensive research have been directed towards enhancing the electrical characteristics of PANI/rGO.[19,20] Consequently, the heightened electrical conductivity and supercapacitance observed in PANI/rGO nanocomposites have facilitated their utilization across diverse fields, including various electronic applications,[21] supercapacitors,[19] energy storage,[22] sensing systems and detectors,[23,24] fuel-cell systems,[25] and numerous other domains.

The synthesis of PANI/rGO nanocomposites conventionally relies on several methods. Electrochemical polymerization involves depositing PANI onto a GO-coated electrode, allowing precise control over thickness and morphology, but is limited to coating applications.[26] Interfacial polymerization polymerizes aniline at the interface of two immiscible liquids, producing high surface area composites but often resulting in heterogeneous and less uniform properties.[27] *In situ* chemical oxidative polymerization is the most commonly used method due to its efficiency. It polymerizes aniline in the presence of GO, which reduces to rGO during the process, ensuring good interaction between PANI and rGO and resulting in improved conductivity and mechanical properties.[28,29] However, achieving higher electrical conductivity requires meticulous optimization of various parameters.[30] These encompass critical factors such as GO filler loading, the oxidant-to-monomer ratio, the nature and concentration of dopant acids, reaction temperature, monomer purity, and polymerization time.[31,32] The traditional approach to optimization, involving the alteration of one parameter at a time, is time-intensive and resource-draining. Conducting numerous experiments, each adjusting a single factor while keeping others constant, consumes considerable time and energy resources. To overcome these limitations, a more efficient approach involves the collective optimization of all pertinent parameters. This is accomplished through an empirical design based on statistical methodologies, illustrated by the implementation of response surface methodology (RSM).[33,34] RSM, combining mathematical and statistical methods, plays a significant role in process modeling and optimization studies.[35] It discerns the impact of independent variables, either in isolation or combination, on the synthesis processes. An inherent strength of RSM lies in its capacity to reduce the number of experiments needed for an in-depth statistical analysis, especially in scenarios involving numerous factors. This modeling approach utilizes polynomials to locally approximate, resulting in the derivation of a mathematical expression that succinctly expresses the complex interplay between the response and the independent variables.[34]

Within the realm of RSM, the Box–Behnken design (BBD) offers significant advantages over the central composite design (CCD) by reducing the number of experimental runs and avoiding extreme factor levels, thus saving valuable time and resources while preventing potentially unsatisfactory or unstable results. Conversely, CCD provides better accuracy for quadratic surface fitting due to its inclusion of axial points but requires more resources and involves extreme conditions, which may not always be practical. Therefore, BBD is more advantageous for preliminary optimization, while CCD is suited for detailed studies.[34,36,37]

Additionally, artificial neural networks (ANN) function as a versatile modeling tool capable of addressing both linear and nonlinear multivariate regression problems across diverse processes, including synthesis and nanocomposite fabrication.[34] Inspired by the biological brain, an ANN begins with the creation of a neural network comprising multiple layers, each housing a defined number of artificial neurons. Each neuron is characterized by a weight and an activation function, where the weights represent the connections between neurons and the activation function mimics the neuron's response. The weight is a crucial parameter that represents the connection between neurons and is optimized during the backpropagation process. Initially, the input data, described by descriptors encapsulating the essential characteristics of the input data, is processed. These descriptors are then multiplied by the corresponding weights and passed through an activation function, effectively initiating a feedforward operation within the network. During the ANN's training phase, the network iteratively adjusts its

© 2024 The Author(s). Published by the Royal Society of Chemistry

Open Access Article. Published on 22 August 2024. Downloaded on 7/19/2025 1:42:39 AM. This article is licensed under a Creative Commons Attribution-NonCommercial 3.0 Unported Licence.

weights through a procedure known as backpropagation, guided by the minimization of the mean square error between the network's predicted output and the actual experimental data. This optimization process is critical for the model to learn the underlying relationships and features within the data effectively. The final steps of ANN modeling involve validating and testing datasets, which are crucial for assessing network performance.[38,39] While ANNs can be computationally expensive and require substantial data and time for training, these limitations can be mitigated through several strategies. Data preprocessing and augmentation, efficient network architectures, advanced optimization algorithms, parallel and distributed computing, and hybrid approaches—such as clustering strategies and combining traditional machine learning techniques with ANNs—can significantly enhance efficiency and performance.[40] These methods ensure that the powerful capabilities of ANNs can be harnessed effectively, even within resource-constrained environments.

Moving beyond experimental design investigations, molecular simulations have become instrumental in guiding researchers in synthesizing intricate materials and understanding mechanisms at the electronic scale. Despite significant efforts to uncover interaction mechanisms with diverse materials, there's an increasing demand for a unified framework that integrates *in situ* nanoscale research, molecular modeling, and their macroscopic implications. Widely embraced computational chemistry techniques, notably density functional theory (DFT), is predominantly applied to predict the electronic structure and ground-state geometries of materials. DFT calculations provide a quantum mechanical description of the electronic distribution within materials, which is fundamental for the understanding of their intrinsic properties. On the other hand, molecular dynamics (MD) simulations are typically employed for simulating the behavior of large systems under real-world conditions, such as varying temperatures and pressures. MD simulations animate the movements of atoms and molecules over time, providing dynamic insights into material behaviors in conditions that closely mimic operational environments.[41,42] These methods, considering certain electron correlation effects at a computationally feasible expense, lay the groundwork for comprehending various chemical processes.[43] Their application in calculating nanocomposite characteristics and interactions with filler materials offers valuable insights into the chemical attributes of these complexes.[44]

A thorough literature review was conducted to pinpoint the key factors influencing the electrical conductivity of PANI/rGO. The investigation revealed that the electrical conductivity of PANI experiences an increase with a higher oxidant molar ratio. Such enhancement in conductivity is attributed to a rise in the density of cation radicals and the extension of PANI chain length. These factors facilitate an enhanced interchain transfer, thereby increasing the carrier mobility.[45] Nevertheless, concentrations of oxidant exceeding 0.5 M resulted in phenazine production, causing a reduction in electrical conductivity.[46,47] Moreover, studies demonstrated an initial increase in PANI conductivity with an aniline amount of up to 0.15 M, followed by a decrease with further additions of aniline.[48] The investigation of the oxidant-to-aniline ratio indicated that an optimal PANI conductivity and yield were achieved with a ratio close to 1. Higher ratios, however, led to over-oxidation, resulting in a decrease in both conductivity and yield.[49] Diverse dopants were explored for their impact on electrical conductivity, showing a positive correlation between dopant concentration and PANI's conductivity.[50] Although, an increase in the dopant/aniline ratio resulted in a notable decline in PANI conductivity, emphasizing the influence of intramolecular mobility of charged species along the chain on electrical conductivity, surpassing the impact of intermolecular hopping within crystalline regions.[51–53] At extremely elevated dopant concentrations, a substantial decline in conductivity was accomplished through concurrent reductions in doping levels and crystallinity.[54] Evaluation of PANI/rGO nanocomposites across different temperatures and rGO loadings demonstrated enhanced conductivity as temperature rises, linked to thermally-assisted charge carrier hopping in disordered materials.[45–48,50,54,55] The integration of rGO into the PANI matrix notably enhanced the conductivity of the nanocomposite. This improvement can be attributed to synergistic interactions between the PANI and rGO phases, involving charge transfer among delocalized P-orbitals.[56] The duration and temperature of the synthesis process played a crucial role in determining the size and structure of PANI/rGO nanocomposites, directly influencing their electrical conductivity. Extended synthesis times and lower temperatures yielded larger and well-defined PANI/rGO systems with enhanced electrical conductivity. Previous studies emphasized that the yield and electrical conductivity remain unaffected by the polymerization temperature when maintained below 0 °C.[54,57] Conversely, elevated temperatures were found to induce more defects, resulting in diminished conductivity.[51] Consequently, a polymerization temperature of approximately 0 °C was considered optimal for the synthesis of PANI/rGO.

In light of the reviewed literature, despite numerous studies on PANI synthesis, a specific optimization of PANI/rGO conductivity using RSM techniques, particularly in scenarios involving the nanoscale, taking into account the interactions and synthesis factors at play, remains unexplored. This study addresses this gap by identifying key factors influencing PANI electrical conductivity, including rGO loading, oxidant-to-monomer molar ratio, and polymerization time. Notably, PANI/rGO was synthesized *via in situ* polymerization in a choline chloride/triethylene glycol-based deep eutectic solvent (DES) acting as an electrolyte. Employing BBD-RSM and ANN methodologies, we systematically assessed various nanocomposite synthesis conditions, analyzing the intricate relationship between electrical conductivity and these factors. Beyond optimization, we conducted a comprehensive analysis of the synthesized nanocomposites using Ultraviolet-visible spectroscopy (UV-vis), photoluminescence spectroscopy (PL), Raman spectroscopy, Fourier-transform infrared spectroscopy (FTIR), X-ray diffraction (XRD), X-ray photoelectron spectroscopy (XPS),

Open Access Article. Published on 22 August 2024. Downloaded on 7/19/2025 1:42:39 AM. This article is licensed under a Creative Commons Attribution-NonCommercial 3.0 Unported Licence.

cyclic voltammetry (CV), and thermogravimetric (TGA) analyses, exploring their structural, optical, and electrochemical properties. Significantly, our tailored computational models for PANI and rGO align with experimental data, enhancing the credibility of our findings. Theoretical analyses, including Frontier molecular orbital (FMO), conductor like screening model for real solvents (COSMO-RS), non-covalent interaction (NCI) based on the reduced density gradient (RDG), and quantum theory of atoms in molecules (QTAIM) deepen our understanding of bonding interactions, providing insights for potential applications in nanocomposite technology. The rationale behind using DES in this study is multi-faceted. First, DES enhances the solubility of reactants, providing a stable medium for *in situ* polymerization, which leads to a more uniform dispersion of rGO within the PANI matrix. DES components, TEG (hydrogen bond donor) and choline chloride (hydrogen bond acceptor), play crucial roles in this process. TEG helps disperse rGO, preventing agglomeration, while choline chloride facilitates the polymerization process and stabilizes the formed nanocomposite. This combination ensures better integration of rGO with PANI, resulting in improved electrical conductivity and mechanical properties of the final composite. Moreover, the use of DES is more environmentally friendly and scalable, making it suitable for industrial applications. This study presents a novel and superior method for synthesizing PANI/rGO nanocomposites, addressing gaps in existing literature and offering a comprehensive optimization strategy for enhanced electrical conductivity.

2. Material and methods

2.1. Materials

Choline chloride (ChCl) ($[(CH_3)_3NCH_2CH_2OH]^+Cl^-$, Sigma-Aldrich, 99%), tetraethylene glycol (TEG) ($HO(CH_2CH_2O)_3CH_2CH_2OH$, Aldrich, 99%), natural graphite powder was consummated by using graphite as a powder with particle size of the order of 10 μm. Sulfuric acid (H_2SO_4, Aldrich, 98%), sodium nitrate ($NaNO_3$, Aldrich, 99%), hydrogen peroxide (H_2O_2, Aldrich, 30%), hydrazine monohydrate (N_2H_4, Sigma-Aldrich, >99%), aniline monomer (ANI)($C_6H_5NH_2$, Sigma-Aldrich, ≥99.5%), ammonium persulfate (APS) ($(NH_4)_2S_2O_8$, Sigma-Aldrich, 98%) was utilized as an oxidant and hydrochloric acid (HCl, Fisher chemical, 37%). All materials were employed in their as-received state, and aniline was saved under refrigeration at 4 °C when not in use.

2.2. Sample preparation

Three different DES formulations were prepared by combining ChCl with TEG in varying molar ratios (1 : 1, 1 : 2, and 1 : 3). The mixtures were heated at 60 °C with continuous stirring. After 30 minutes, the resulting DESs became a homogeneous colorless liquid. Fig. 1 provides a schematic representation of the DES preparation process. Only the DES with a 1 : 2 molar ratio exhibited stability and was selected for further experimentation. The preparation of GO is followed our prior work[58,59] and for the reduction of GO to rGO, a hydrazine chemical reduction method was then employed.

The synthesis of PANI/rGO nanocomposites was carried out according to previously established procedures.[60,61] Initially, a dispersion of rGO was prepared by weighing the appropriate amount, adding distilled water, and subjecting it to ultrasonication for 1 hour. Simultaneously, an APS solution was prepared by dissolving it in a fresh 1 M HCl/30% DES solution. The DES concentration is crucial to retain its properties and ensure that the synthesis of the composites is facilitated by the DES serving as an electrolyte,[62] rather than the individual effects of TEG and ChCl in solution. The synthesis of PANI/rGO commenced with the dissolution of pure aniline and rGO in the 1 M HCl/30% DES solution, forming an aniline-rGO suspension. This suspension was ultrasonicated for 20 minutes and then placed in an iced bath, maintaining a temperature range of 0–5 °C while being mechanically stirred (as depicted in Fig. 1). The APS solution was carefully added drop by drop to the aniline-rGO suspension in a two-step process to prevent excessive temperature elevation. The oxidant-to-aniline ratio was meticulously controlled throughout the synthesis. Approximately 20–30 minutes after the initial addition of the oxidant, the solution's color transitioned from blackish-blue to progressively greener, indicating the progression of the reaction. The resultant nanocomposites and pure PANI were separated by centrifugation, thoroughly washed with 1 M HCl, fresh distilled water, and acetone, and subsequently dried in an oven at 50 °C for 48 hours. Details regarding the polymerization time, the aniline-to-rGO ratio, and the aniline-to-APS ratio are provided in the experimental design strategy outlined below.

2.3. Experimental design by response surface methodology

Data analysis investigation is a valuable tool for uncovering concealed insights and constructing predictive models. The RSM, initially introduced by Box and Wilson,[35] stands out as a robust approach for scrutinizing interactive influences within a system and for optimizing its performance. RSM typically employs specific experimental designs, with the most commonly employed ones being the Box–Behnken design (BBD) and the central composite design (CCD).[35] In the context of this study, we employed the BBD design to explore the impact of variables such as molar ratio of APS/ANI, rGO loading, and polymerization time on the electrical conductivity of PANI/rGO-based nanocomposites. Within the BBD framework, each factor is systematically assigned one of three equidistant values. The experimental conditions are represented by points positioned at the midpoint of the edges in the experimental space, which can be visualized as a cube, as well as at the center (as depicted in Fig. 2).

The total number of experiments, N, the variables under consideration, k, and the central points, C_0, can be calculated using the following eqn (1):

$$N = 2k\,(k - 1) + C_0 \quad (1)$$

Table 1 provides an overview of the experimental design using the BBD model. This design incorporates three factors, each with three levels, and we have included both actual and

 © 2024 The Author(s). Published by the Royal Society of Chemistry

Open Access Article. Published on 22 August 2024. Downloaded on 7/19/2025 1:42:39 AM.
This article is licensed under a Creative Commons Attribution-NonCommercial 3.0 Unported Licence.

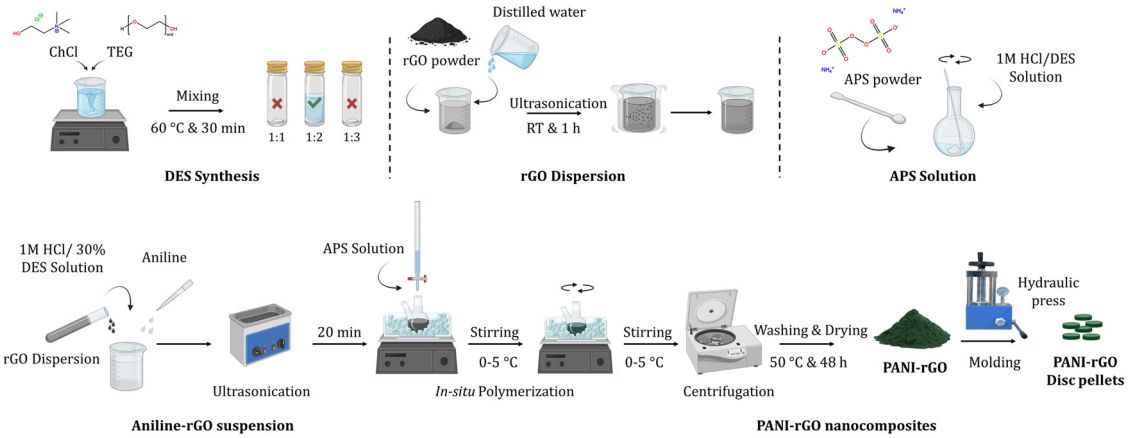

Fig. 1 Flowchart illustrating of the experimental methodology used in this work.

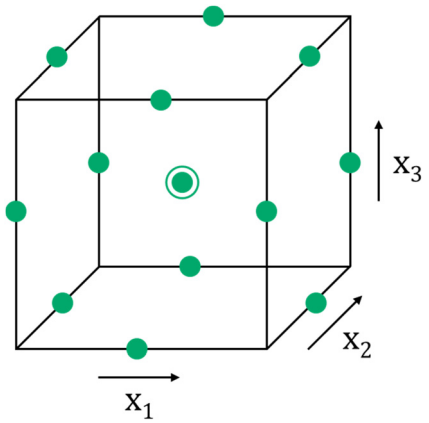

Fig. 2 Configuration of the Box–Behnkendesign for a three-factor system.

Table 1 Factors Investigated in the Box–Behnken design experiment

		Levels		
Factors	Coded	−1	0	1
Molar ratio of APS/ANI	X_1	0.25	0.5	0.75
rGO loading (wt%)	X_2	1	3	5
Time (h)	X_3	2	4	6

coded values for better understanding. The three optimized independent variables are APS/ANI ratio (X_1), rGO loading (X_2), and polymerization time (X_3). For each independent variable, we employed a horizontal encoding scheme, which assigns three values: −1, 0, and +1, facilitating a systematic exploration of the experimental space. The actual ranges for these variables are: APS/ANI ratio (X_1) from 0.25 to 0.75, rGO loading (X_2) from 1 to 5 wt%, and polymerization time (X_3) from 2 to 6 hours. The selected range of rGO loadings (1, 3, and 5 wt%) was based on a combination of literature evidence and systematic pilot experimentation. Literature suggests that rGO loadings within this range effectively enhance the electrical and mechanical properties of PANI/rGO nanocomposites. Pilot experiments conducted with rGO loadings below 1 wt% showed minimal improvements in properties, while loadings above 5 wt% led to processing difficulties due to increased viscosity and rGO aggregation. Therefore, the chosen range optimally enhances the properties of PANI/rGO nanocomposites while maintaining good processability.[26,63–65]

The relationship and interactions between the independent variables and the response factors were thoroughly investigated using a second-order polynomial equation (eqn (2)):

$$y = \beta_0 + \sum_{j=1}^{k} \beta_j X_j + \sum_{j=1}^{k} \beta_{jj} X_j^2 + \sum_{i<j}^{k} \beta_{ij} X_i X_j \qquad (2)$$

Here, y represents the predicted value of the response, β_0 is the offset term, j, ij, and jj correspond to the linear coefficients, the cross-product coefficients, and the quadratic coefficients, respectively. X_i and X_j are the independent factors. To carry out this analysis, we employed JMP SAS Pro® 16 software. This robust software facilitated the evaluation of experimental data and the execution of analysis of variance (ANOVA) to ascertain the model's fitting accuracy. This statistical analysis is essential for understanding the impact and significance of the independent variables on our response factors.

2.4. Artificial neural network

Artificial neural networks (ANNs) are computational frameworks inspired by the structure of the biological nervous system. They include diverse architectures such as feedforward networks, radial basis function networks, and fuzzy networks.[38,39] As demonstrated *via* Hornik *et al.*,[66] multilayered feedforward networks, even with just one hidden layer, possess the capability to accurately approximate any function from n dimensions to m dimensions. In recent years, ANNs have revolutionized engineering by offering unparalleled predictive and estimation capabilities, surpassing conventional modeling approaches like RSM concerning predictive precision.[67,68] In

Open Access Article. Published on 22 August 2024. Downloaded on 7/19/2025 1:42:39 AM. This article is licensed under a Creative Commons Attribution-NonCommercial 3.0 Unported Licence.

the present study, we harnessed the power of ANNs to predict the intricate, non-linear relationship between our input parameters (X_1, X_2, and X_3) and the response variable (y), utilizing an experimental dataset derived from the BBD design. Our network architecture was meticulously constructed using JMP SAS Pro® 16 software (SAS Institute, Cary, NC), ensuring the efficacy of the feed-forward ANN. The configuration of the neural network holds a pivotal role in shaping the ANN model's capacity for generalization. It essentially comprises three key layers: input, hidden, and output, with each layer accommodating an array of neurons. The quantity of neurons in the input and output layers directly corresponds to the count of input and output variables. Consequently, we evaluated eight different ANN architectures, each equipped with a single hidden layer containing varying neuron counts ranging from 3 to 24. To ensure the model's robustness and reliability, we divided our datasets into training and testing subsets, following an 80% : 20% ratio. This strategy allowed us to systematically explore various ANN architectures, ultimately selecting the optimal setup based on superior performance with the testing dataset. The equations within the ANN model incorporate various parameters that elucidate the neural network's behavior. These parameters encompass the weights (W_m) connecting neurons, the inputs (x) to specific neurons (n), considerations of the hidden layer (l), and the biases (b) associated with each neuron. Additionally, we incorporated the hyperbolic tangent ($\tan h$) function into the expressions, effectively confining the output of each neuron to the variety of [−1, 1]. This interval signifies the extent of activation or deactivation, ensuring meticulous control over the network's dynamics and results. The mathematical representation of the output of neuron (j) arises from the synergistic interplay of these parameters:

$$H_{n,l} = \tanh\left(\sum_{m=1}(W_{m,n,l})(X_{n,l})b_{n,l}\right) \quad (3)$$

To assess the effectiveness of both ANN and RSM models, performance metrics including root mean square error (RMSE), coefficient of determination (R^2), average absolute relative deviation (AARD), and mean absolute error (MAE) were applied where their expressions are shown in eqn (4)–(7), respectively. Where σ_{exp}, σ_{pred}, and $\bar{\sigma}$ indicate the experimental, predicted, and average values, while p denotes the total count of experimental data points.

$$R^2 = 1 - \frac{\sum_1^p (\sigma_{exp} - \sigma_{pred})^2}{\sum_1^p (\sigma_{exp} - \bar{\sigma})^2} \quad (4)$$

$$\mathrm{RMSE} = \sqrt{\frac{\sum_1^p (\sigma_{exp} - \sigma_{pred})^2}{p}} \quad (5)$$

$$\mathrm{AARD}\,(\%) = \frac{100}{p} \times \sum_1^p \frac{|(\sigma_{pred} - \sigma_{exp})|}{\sigma_{exp}} \quad (6)$$

$$\mathrm{MAE} = \frac{1}{p}\sum_1^p |\sigma_{pred} - \sigma_{exp}| \quad (7)$$

2.5. Characterization and morphology

The Ultraviolet-visible (UV-vis) were recorded with V-650 JASCO spectrophotometer equipped with an integrating sphere. The photoluminescence (PL) investigation was carried out on the spectrofluorometer HORIBA FL3-DFX-iHR320 model. Raman was recorded with an invia microscope spectrometer (RENISHAW). Fourier-transform infrared (FTIR) spectroscopy was analyzed by the V-650 JASCO spectrophotometer equipped with an integrating sphere. X-ray diffraction (XRD) analysis was performed with Cu Ka X-ray sources on a D/Max-2400 powder diffractometer (Japanese Physical Company). The surface analysis of the synthesized materials was examined through means of an X-ray Photoelectron Spectroscopy (XPS) (Escalab THERMO SCIENTIFIC).

Cyclic voltammetry (CV) experiments were performed utilizing a Volta Lab PGZ 301 apparatus with Volta Master 40 software, employing a standard three-electrode configuration. The setup comprised a counter electrode made of platinum, a reference electrode of Ag/AgCl, and a working electrode made of platinum with modifications. A solution of 0.1 M lithium perchlorate ($LiClO_4$) in dimethylformamide (DMF) served as the electrolyte support in the analytical protocol. The electrochemical performances of PANI/rGO nanocomposites were explored through CV within a potential window with a range of −0.8 V to 1.6 V.

Thermal stability study of the PANI/rGO nanocomposites were conducted under nitrogen atmosphere (N_2) at room temperature up to 1000 °C with a heating rate of 10 °C minutes through thermogravimetric (TGA) analysis.

2.6. Electrical conductivity measurements

The four-point probe method was employed to assess the electrical conductivity of pure PANI, rGO, and PANI/rGO nanocomposites. Digital micrometers were used to determine the thickness of the samples, which were shaped into discs with a diameter of approximately 12 mm. The electrical measurements were performed using a Keithley 195 current source and a Keithley 197 electrometer, both computer-controlled. For these measurements, the disc pellet samples were placed on an insulated test bed, connected to a PRF-912 probe model. This test was primarily focused on quantifying the sample's surface resistance. The reciprocal of resistivity (ρ) determined the electrical conductivity (σ) of the disc pellet samples, as expressed in eqn (8):

$$\sigma = \frac{1}{\rho} \quad (8)$$

where σ represents electrical conductivity in Siemens per centimeter (S cm^{-1}), while ρ denotes resistivity measured in ohm-centimeters (Ω cm).

2.7. Computational methodology

This study involved comprehensive calculations concerning geometric parameters, internal energies, and electronic

 © 2024 The Author(s). Published by the Royal Society of Chemistry

Open Access Article. Published on 22 August 2024. Downloaded on 7/19/2025 1:42:39 AM. This article is licensed under a Creative Commons Attribution-NonCommercial 3.0 Unported Licence.

properties of the nanocomposite. Initially, we utilized the Material Studio software[69,70] to perform MD simulations aimed at assessing the interaction energy between the PANI molecule and rGO sheet. The initial simulation box was constructed by placing the rGO sheet alongside the PANI molecule to investigate the inherent interactions between these components. Accordingly, the box's geometry was optimized to relax the entire molecular system. Subsequently, the box underwent NVT dynamics for approximately 2000 picoseconds, utilizing a 1 femtosecond time step at a temperature of 298 kelvin. These simulations employed the COMPASS forcefield.[71] After the NVT dynamics, a second MD simulation was conducted using the NPT thermodynamic ensemble for 20 000 picoseconds, also with a 1 femtosecond time step at 298 kelvin. The outcome of this simulation led to another round of geometric optimization.[70,72] Energies were calculated for approximately of a hundred resulting conformations or more. Among these conformations, the one with the lowest energy was selected as the model for subsequent analysis. The selected model was further optimized *via* the DFT M06-2X functional[70,73–77] and the TZVP basis set,[78–80] and this optimization was carried out with the Turbomole software.[81–85] To delve deeper into the characteristics of the PANI/rGO system and their interactions, the conductor-like screening model for real solvents (COSMO-RS) methodology was applied. This involved utilizing the COSMOthermX program to calculate relevant thermodynamic parameters. The COSMO-RS calculations were conducted at 298.15 K to ensure that the computational data accurately reflects the real-world behavior of the system. In addition, the optimization process allowed us to determine geometrical parameters as well as various QTAIM and RDG topological parameters.

To represent the PANI conducting polymer, an oligomer was employed, comprising four monomer units of aniline. This oligomer includes 4 phenyl rings and a total of 48 atoms. In our model, rGO was selected. It's composed of 55 carbon atoms and 11 oxygen atoms, with open ends saturated by hydrogen atoms. rGO is essentially the reduced form of GO, featuring oxygen-containing groups like carboxyl acid (–COOH), hydroxy (–OH), and epoxy (–O–) functional groups that are haphazardly affixed to the edges and surface. The portrayal of rGO's structure lacks precision due to the erratic distribution of these oxygen-containing functional groups and the notable structural disarray within the framework.[86] Both rGO and PANI underwent neutral optimization. This optimization allowed us to determine various electronic properties, including charge distribution, energies associated with the highest and the lowest occupied molecular orbitals (HOMO and LUMO, respectively), as well as band gap (E_g), which was estimated using the HOMO and LUMO energies through the following equation (eqn (9)):

$$E_g = E_{LUMO} - E_{HOMO} \quad (9)$$

To comprehensively investigate weak interactions within a three-dimensional framework, our study employs an illuminating approach focused on the analysis of NCI.[87–89] Several theoretical models, including NCI-RDG and QTAIM, were applied. The RDG analysis relies on fundamental electron density (ρ) and reduced density gradients (RDGs), expressed in mathematical terms using eqn (10), where ρ denotes the electron density, and $\nabla\rho$ signifies its initial derivative. This method is particularly effective for identifying van der Waals interactions and weak non-covalent interactions, including hydrogen bonding and steric repulsions, which become significant at specific distances and can significantly influence the system as a whole.[90,91]

$$s = \frac{1}{2(3\pi^2)^{1/3}} \frac{|\nabla\rho|}{\rho^{4/3}} \quad (10)$$

For NCI analyses based on the RDG and QTAIM, we incorporated the Molden input from Turbomole[92] and utilized the computational tool Multiwfn[93] to explore and identify potential weak interactions within the analyzed system. To visualize the results, we generated RDG plots and QTAIM maps *via* the Visual Molecular Dynamics (VMD) interface.[94] Furthermore, color scatter plots were created with the assistance of gnuplot.[95] These advanced computational techniques facilitated an in-depth examination of weak interactions within the system under investigation.

3. Results and discussion

3.1. Response surface methodology results

In this investigation, a series of 15 experiments was executed using RSM-BBD, involving three repeated experiments that incorporated three input variables and three center points. Each experiment was replicated twice, and the mean value was determined. The design matrix for the experiments and the predicted outcomes are detailed in Table 2. Notably, the center point runs (#4, #10, and #15) exhibited minimal variations in the electrical conductivity, indicative of excellent experimental repeatability.

Table 2 RSM-BBD design matrix with its corresponding responses of electrical conductivity

	Code values			Real values			Electrical conductivity
#Run	X_1	X_2	X_3	X_1	X_2	X_3	$\sigma \times 10^{-3}$ (S cm^{-1})
1	+	−	0	0.75	1	4	3.142
2	0	−	−	0.5	1	2	3.203
3	0	+	+	0.5	5	6	2.958
4	0	0	0	0.5	3	4	2.472
5	−	0	−	0.25	3	2	2.189
6	−	+	0	0.25	5	4	1.756
7	−	0	+	0.25	3	6	2.277
8	−	−	0	0.25	1	4	1.893
9	0	+	−	0.5	5	2	2.122
10	0	0	0	0.5	3	4	2.250
11	0	−	+	0.5	1	6	3.739
12	0	0	0	0.75	5	4	3.295
13	+	0	−	0.75	3	2	3.715
14	+	0	+	0.75	3	6	**4.975**
15	0	0	0	0.5	3	4	2.122

Open Access Article. Published on 22 August 2024. Downloaded on 7/19/2025 1:42:39 AM. This article is licensed under a Creative Commons Attribution-NonCommercial 3.0 Unported Licence.

Furthermore, a comprehensive evaluation of the experimental outcomes involved an in-depth analysis of multiple regression models. After assessing various models, the quadratic model emerged as the most suitable fit for all design points. To understand the effects of the variables and their interactions, Analysis of Variance (ANOVA) was performed, and the findings are reported in Table 3. It was observed that a linear effect (X_1) and a quadratic effect (X_3^2) were statistically significant, with a p-value < 0.05. Nevertheless, the other linear and interaction terms, along with all quadratic terms, were considered statistically insignificant (p-value > 0.05). The experimental data exhibited a favorable agreement with the formulated model equation, evident from the lack of fit result with a p-value > 0.05. Subsequently, a second-order polynomial function, represented by eqn (8), was deduced to approximate the σ of PANI/rGO nanocomposites:

$$\sigma = 2.28144 + 0.87651X_1 - 0.23076X_2 + 0.33983X_3 + 0.07224X_1X_2 + 0.29292X_1X_3 + 0.07501X_2X_3 + 0.26177X_1^2 - 0.02154X_2^2 + 0.74556X_3^2 \quad (11)$$

Here, σ, X_1, X_2, and X_3 represent the electrical conductivity of PANI/rGO nanocomposites, coded forms of the APS/ANI ratio, rGO loading, and the time of polymerization, respectively.

The results from the ANOVA analysis, presented in Table 3, reveal an exceptionally low p-value (<0.0001), signifying a highly significant alignment of the model with the experimental data. Moreover, the lack of fit value (0.1212) substantiates the model's aptitude in capturing the experimental trends, thereby confirming its *bona fide* predictive power. Moreover, the model demonstrates excellent predictive performance, supported by the elevated adjusted and predicted R^2 values of 0.8041 and 0.9301, respectively, highlighting the precision and dependability of its predictions.

Additionally, to verify the adequacy of the model and ensure it meets the analysis assumptions, residual analysis was conducted. Given the dispersion of residuals observed in Fig. 3, the data points scatter randomly about the center line, devoid of any apparent systematic trends or patterns. This randomness is indicative of the model's adequacy in capturing the inherent variability of the experimental data. Furthermore, the scatter of residuals displayed uncorrelated and random distribution on both sides of the center line, indicating constant variance. These robust findings provide compelling evidence that the model is appropriate and indeed satisfies the assumptions of the analysis.

Table 3 Statistical analysis (ANOVA) for the quadratic model of electrical conductivity in PANI/rGO nanocomposites

Parameter	D_f	Sum of squares	Mean square	F ratio	Prob. $> F$
Intercept	9	10.123	1.125	7.3866	0.0002[a]
X_1 (molar ratio of APS/ANI)	1	6.147	6.147	40.3646	0.0014[a]
X_2 (rGO loading)	1	0.426	0.426	2.7974	0.1553
X_3 (time)	1	0.924	0.924	6.0671	0.057
X_1X_2	1	0.021	0.021	0.1371	0.7264
X_1X_3	1	0.343	0.343	2.2538	0.1936
X_2X_3	1	0.023	0.023	0.1478	0.7165
X_1^2	1	0.253	0.253	1.6615	0.2538
X_2^2	1	0.002	0.002	0.0113	0.9196
X_3^2	1	2.052	2.052	13.4778	0.0144[a]
Lack of fit	3	0.699	0.233	7.4106	0.1212
Pure error	2	0.063	0.031		
Total	14	10.885			

[a] Significant at 95% confidence interval.

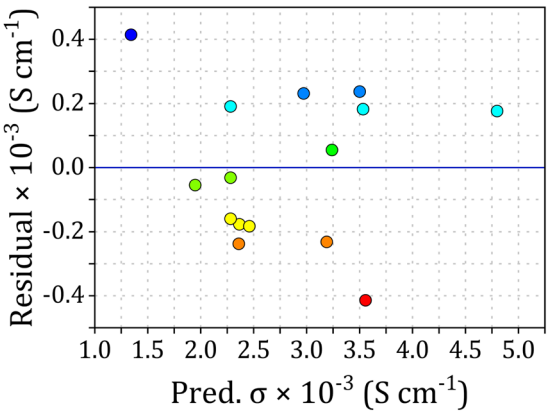

Fig. 3 Correlation between residuals and predicted values for the electrical conductivity of PANI/rGO nanocomposites.

To understand the interaction effects of two variables while maintaining the other variables at their central point value (zero level), we created 2D contour and 3D surface plots using eqn (11). Fig. 4(A) and (D) depict the influence of the APS/ANI ration and rGO loading at a constant polymerization time of 4 h. It is evident that the electrical conductivity increases as the APS/ANI ratio and rGO loading vary from 0.5 to 0.75 and 3 to 5 wt%, respectively. However, at higher APS/ANI ratios and increased rGO loading, the electrical conductivity shows a decreasing trend. This behavior can be attributed to the increased amount of APS (oxidant), resulting in the generation of a higher number of radical cations, which consequently accelerates the chemical oxidative polymerization of ANI. As acknowledged, the electrical conductivity of PANI is contingent on the protonation degree or the effective conjugation length of PANI chains.[96] In addition, the higher content of rGO in the nanocomposites hinders the orderly arrangement of PANI chains, inducing a higher structural disorder and creating more conjugated defects, ultimately contributing to lower conductivity.[56] Likewise, Fig. 4(B) and (E) exhibit the combined impact of APS/ANI ratio and polymerization time (h) on electrical conductivity while keeping the rGO loading fixed at 3 wt%. It is evident that electrical conductivity continues to rise with an increase in the polymerization time, consistent with previous reports.[33,97] Finally, Fig. 4(C) and (F) demonstrate the linear influence of rGO loading and polymerization time on the electrical conductivity, suggesting their minor impact on the overall electrical conductivity.

3.2. Artificial neural network modeling

In this study, ANN was constructed to capture the intricate nonlinear associations among three independent variables (molar ratio of APS/ANI, rGO loading, and polymerization time) and

© 2024 The Author(s). Published by the Royal Society of Chemistry

Open Access Article. Published on 22 August 2024. Downloaded on 7/19/2025 1:42:39 AM.
This article is licensed under a Creative Commons Attribution-NonCommercial 3.0 Unported Licence.

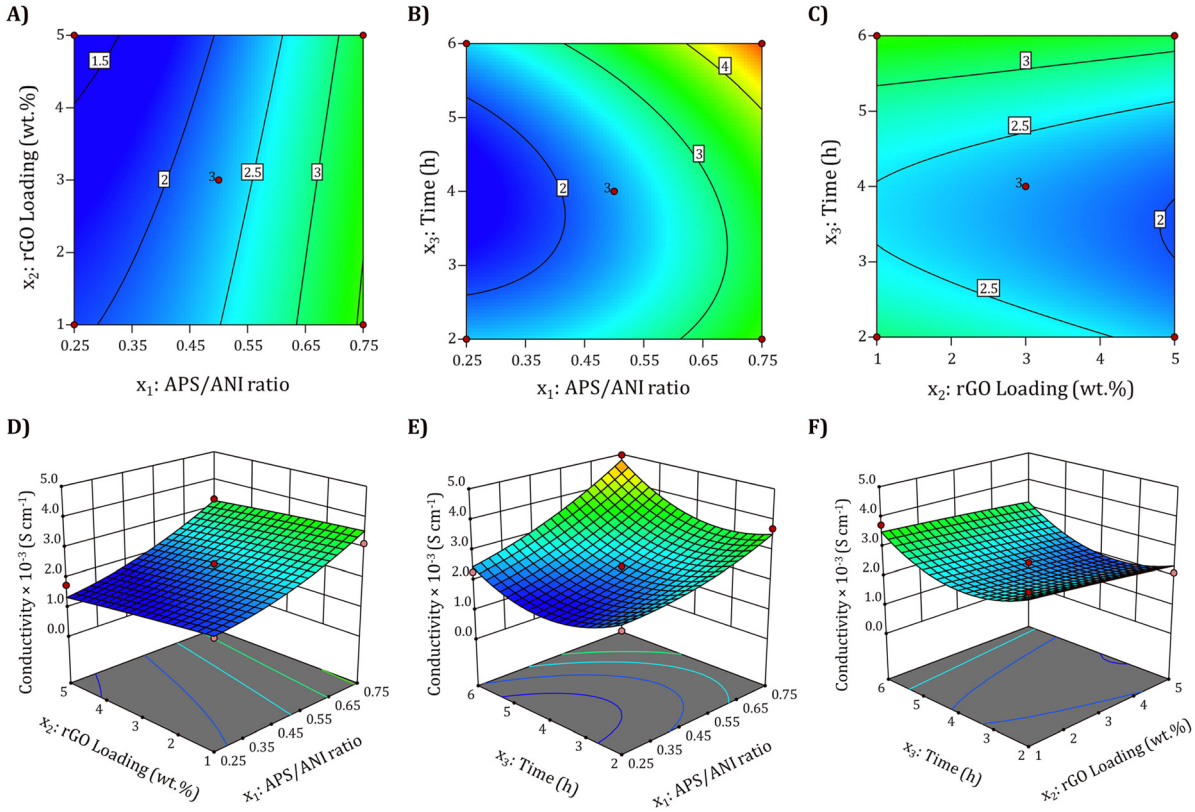

Fig. 4 Two-dimensional (2D) contour and three-dimensional (3D) surface plots illustrating the combined impact on electrical conductivity. Interplay of APS/ANI ratio and rGO loading (A) and (D), APS/ANI ratio and polymerization time (B) and (E), and rGO loading and polymerization time (C) and (F).

the desired output (electrical conductivity) through the application of the Broyden–Fletcher–Goldfarb–Shanno (BFGS) algorithm. For performance optimization, we meticulously tuned hyperparameters, training and assessing a total of eight distinct ANN architectures. We systematically varied the number of neurons in a hidden layer to identify the configuration that yielded the lowest RMSE and the highest R^2 values following this analysis, we determined the final architecture of the ANN model, adopting a 3-12-1 configuration, where the hidden layer comprises 12 neurons. Fig. 5(A) illustrates the statistical metrics RMSE and R^2 for different architectures, revealing that the 3-12-1 architecture yields lower RMSE and higher R^2 values, indicating superior predictive performance. The proposed ANN structure is schematically depicted in Fig. 5(B).

3.3. Comparison between RSM and ANN models

The effectiveness of the proposed approaches has been validated, establishing the superiority of the methods in depicting the electrical conductivity of PANI/rGO nanocomposites. To compare the predictions of the respective models (RSM-BBD and ANN), a comprehensive error analysis was performed, and key performance metrics, including R^2, RMSE, AARD, MAE, and

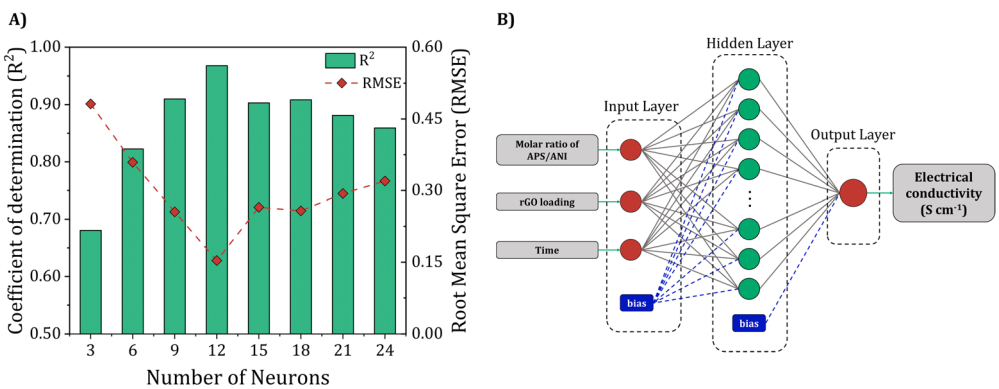

Fig. 5 (A) Performance of the developed ANN model with respect to the neurons' number in the hidden layer, and (B) schematic representation of the 3-12-1 ANN architecture.

Open Access Article. Published on 22 August 2024. Downloaded on 7/19/2025 1:42:39 AM.
This article is licensed under a Creative Commons Attribution-NonCommercial 3.0 Unported Licence.

relative deviation (RD%), were computed using the equations detailed in the methodology section. As depicted in Fig. 6(A) and (B), the scatter plots for both models illustrated strong concordance with the experimental data, substantiated by the elevated R^2R^2 values of 0.93 and 0.97 for RSM and ANN, respectively. Notably, the ANN demonstrated superior accuracy in fitting the experimental data when contrasted with the RSM model, as indicated by the plot of RD% in Fig. 6(C). This higher predictive accuracy of the ANN model highlights its superior performance.

However, it is crucial to recognize that the ANN model, in its standard form, does not inherently elucidate the influence of input parameters on the response; this understanding typically necessitates further analysis, such as a query strategy for selecting informative training data or post-hoc interpretability methods. In contrast, the primary advantage of RSM lies in its capacity to demonstrate factor contributions through coefficients in the regression model.

The integration of ANN techniques in our study enhanced the predictive accuracy of electrical conductivity, achieving a conductivity of 4.988×10^{-3} S cm^{-1}, compared to 4.975×10^{-3} S cm^{-1} obtained using RSM. Although the numerical enhancement of 0.013 mS cm^{-1} may appear modest, it is significant for several reasons.

First, the improvement from ANN demonstrates superior predictive capability over RSM. Evaluation metrics listed in Table 4, including R^2, AARD, and RMSE, provide additional validation of the robust alignment between the ANN-predicted and experimental values, surpassing the performance achieved by the RSM model. The enhanced predictive prowess of ANNs can be ascribed to their adeptness in approximating non-linear systems, a capability beyond the scope of RSM, which is confined to approximating systems using second-order polynomials.

Table 4 Comparative assessment of predictive performance between RSM and ANN models

	Model	
Metric	BBD	ANN (3-12-1)
R^2	0.9301	0.9675
RMSE	0.3902	0.1535
AARD (%)	7.68	2.86
MAE	0.1985	0.0797

Enhanced predictive accuracy results in better reproducibility in large-scale production. The precise optimization of parameters ensures that the synthesized nanocomposites consistently achieve high performance, reducing variability and enhancing reliability. In practical applications, even small improvements in conductivity can significantly impact the overall performance of materials. Higher conductivity improves the efficiency of electronic devices and sensors, leading to better sensitivity and faster response times. For industrial applications, achieving minor enhancements in material

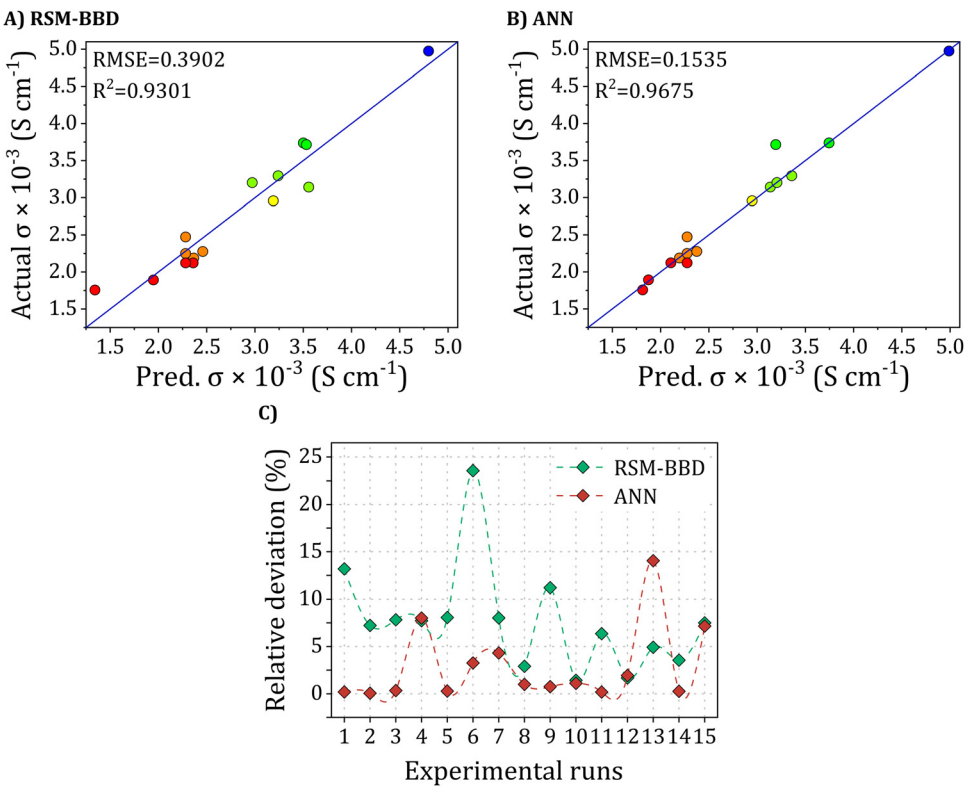

Fig. 6 Regression analysis between actual and predicted electrical conductivity using (A) RSM-BBD and (B) ANN models, and (C) relative deviation plot for the predictions of electrical conductivity by RSM-bbd and ANN models.

© 2024 The Author(s). Published by the Royal Society of Chemistry

Open Access Article. Published on 22 August 2024. Downloaded on 7/19/2025 1:42:39 AM. This article is licensed under a Creative Commons Attribution-NonCommercial 3.0 Unported Licence.

properties can have a substantial cumulative effect. Enhanced conductivity can lead to cost savings, improved product quality, and competitive advantages in the marketplace.

3.4. Electrical conductivity optimization of the PANI/rGO nanocomposites

In our endeavor to improve the electrical conductivity of PANI/rGO nanocomposites, we harnessed the power of a response surface optimization approach and ANN predictive model. These methodologies are intricately crafted to identify the optimal position within the design space, whether it involves a minimum, a maximum, or a specific region characterized by a stable response. The main objective in this investigation was to maximize the electrical conductivity of PANI/rGO nanocomposites. To accomplish this, we relied on the RSM and ANN models. Through meticulous analysis, we uncovered the precise conditions that lead to the highest electrical conductivity. These optimal conditions were revealed to be an APS/ANI molar ratio of 0.75, an rGO loading of 3 wt%, and a polymerization time of 6 hours.

Following this optimization, a comprehensive analysis using various techniques, encompassing UV-visible, Raman, FTIR, PL, XRD, XPS, CV, and TGA analyses were performed for the PANI/rGO samples. These analyses provided in-depth insights into the structural, optical, and electrochemical performances of the investigated PANI/rGO nanocomposites.

3.5. Compositional and structural analyses

3.5.1. UV-visible spectroscopy. Extensive investigations have been undertaken to comprehensively analyze the optical properties of PANI/rGO (1, 3, and 5 wt%) nanocomposites, as depicted in Fig. 7. The UV-Visible spectrum of pure PANI, revealed in Fig. 7(A), unveils the existence of two significant absorbance peaks around 270 nm and 655 nm. The initial peak at 270 nm is attributed to the π–π* electron orbital transition of the benzenoid ring within PANI structure. This transition reflects the movement of electrons within the conjugated system, shedding light on the electronic properties associated with the benzenoid moiety.[21,98] On the other hand, the UV-Vis spectrum of rGO demonstrates enhanced and uniform absorption spanning the range of 240 to 800 nm, indicating the occurrence of a restricted number of oxygen groups or graphitic domains on the graphene planes. This observation can be attributed to the n → π* transition arising from the occurrence of C=O bonds in carbonyl or carboxyl groups within rGO, which occur as a result of partial reduction.[64] This absorbance profile is characteristic of graphene materials and indicates the restoration of electronic conjugation within rGO sheets.[99,100] The enhanced absorption and absence of distinct peaks within this range indicate the formation of a continuous, highly conjugated graphene structure in rGO. Regarding the PANI/rGO nanocomposites in varying ratios, it is noteworthy that compared to the pure PANI or rGO samples, it displays three robust absorbance peaks at 210 nm, 270 nm, and 655 nm, each showing a shift with respect to the peaks observed in the pure materials. These peaks are shifted, suggesting a relatively complex interaction between PANI and rGO. The observed peak at approximately 210 nm is attributed to a π–π* aromatic transition.[101] The wide peak ranging from 240 to 320 nm in the PANI/rGO spectra is associated with the benzenoid π–π* transition. Additionally, a shoulder is observed, likely stemming from the Polaron–π* transition of quinoid-imine functional groups due to protonation. These findings affirm the

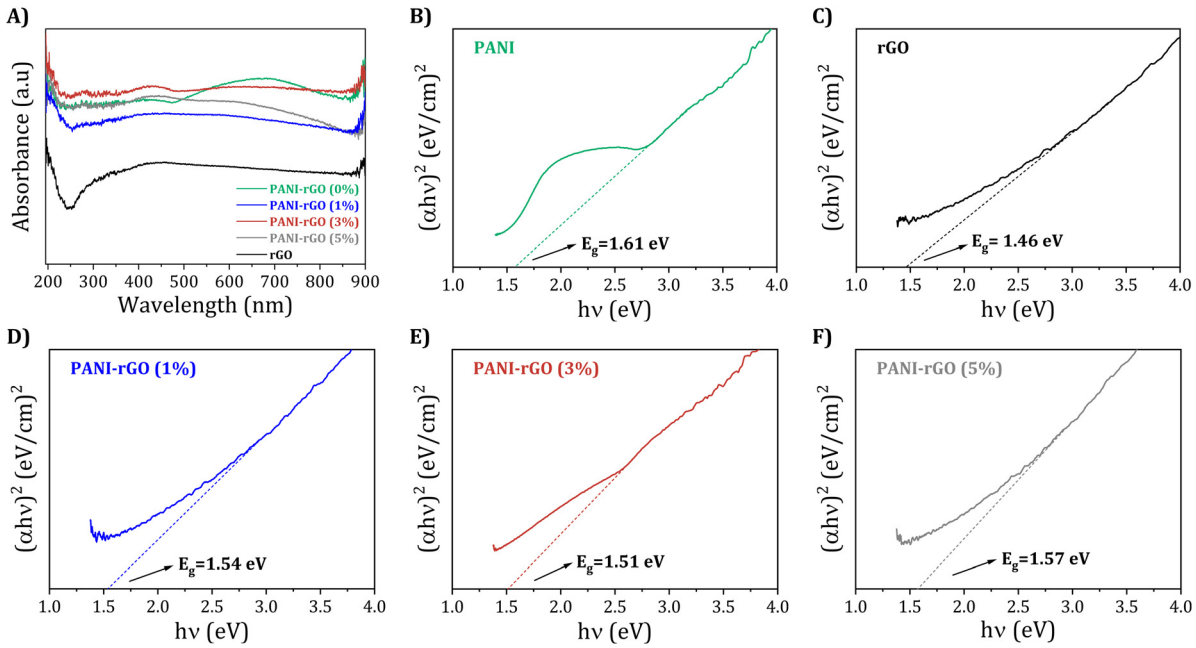

Fig. 7 (A) UV-Visible adsorption spectra (A) with its corresponding Tauc plots for pure PANI, rGO, and PANI/rGO nanocomposites (B)–(F).

Open Access Article. Published on 22 August 2024. Downloaded on 7/19/2025 1:42:39 AM.
This article is licensed under a Creative Commons Attribution-NonCommercial 3.0 Unported Licence.

presence of diverse interactions, involving hydrogen bonding and π–π coordination among the PANI and rGO.[102–104]

Moving on, Fig. 7(B–F) show the corresponding Tauc plot, $(\alpha h\nu)^2$ with hν, for pure PANI, rGO, and PANI/rGO (1, 3, and 5 wt%) samples, with h representing the Planck constant and ν denoting the frequency. The energy gap (E_g) can be estimated by determining the x-intercept of the extrapolated Tauc plot.[105] For pure PANI and rGO, the band gap is found to be approximately 1.61 and 1.46 eV, respectively (Fig. 7(B and C)). Furthermore, as the rGO loading increases up to 3 wt%, the optical band gap of the composite decreases to 1.51 eV. In PANI/rGO nanocomposites, the integration of rGO leads to the formation of new energy levels known as trap states. These states are typically located near the valence band and arise due to the complex interaction between PANI and rGO, introducing localized states or defect levels within the composite structure. These trap states play a pivotal role in the electronic properties of the nanocomposite (Fig. 7(D and E)). While electron delocalization within the conjugated PANI chains is a contributing factor, the primary mechanism for the reduced energy gap (E_g) and increased conductivity lies in these trap states. These states provide a pathway for electrons to move from the valence band to the conduction band with minimal energy input. Essentially, the trap states create a 'stepping stone' effect, allowing electrons to 'hop' between these states. This hopping mechanism is less energy-intensive than the direct transition across the full band gap in a pristine material. As a result, the presence of these trap states in PANI/rGO nanocomposites facilitates easier and more efficient electron movement, leading to enhanced electrical conductivity. However, it is important to note that this is a nuanced balance. An excessive concentration of trap states or rGO can lead to increased scattering and localization effects, potentially countering the benefits of enhanced conductivity. Nevertheless, as shown in Fig. 7(F), with a continued increase in rGO loading (5 wt%), barriers are formed within the PANI chain, hindering electron delocalization and resulting in a corresponding increase in the band gap (1.57 eV).[56] Thus, incorporating 3 wt% rGO into the PANI matrix promotes electron delocalization, broadening the absorption range, and enhancing electrical conductivity.[106,107] Meanwhile, the reduction in the energy gap compared to rGO alone is particularly significant which expands the absorption range into the visible area of the electromagnetic spectrum, thereby improving the light harvesting efficiency of PANI/rGO nanocomposites. Consequently, the incorporation of rGO facilitates increased delocalization of electrons within the PANI chains, allowing for the absorption of a wider range of photons.[108] As a result, the PANI/rGO nanocomposites exhibit improved electrical conductivity, as observed in the present study.

3.5.2. Photoluminescence studies (PL). Photoluminescence (PL) spectra provide valuable insights into the recombination efficiency of photo-generated electrons and holes, which can be inferred from the fluorescence intensity. A strong PL intensity signifies a rapid recombination of photo-generated charge carriers with a short lifetime. Conversely, a higher separation efficiency of the photo-generated carriers, *i.e.*, electrons (e^-) and holes (h^+), resulting in longer lifetimes, leads to a reduction in the intensity observed in the PL spectra.[109] Fig. 8 illustrates the PL spectrum of pure PANI, rGO, as well as rGO-PANI nanocomposite samples (1, 3, and 5 wt%), recorded using an excitation wavelength of 320 nm. The PL spectrum for pure PANI exhibits two broad peaks in the wavelength range of 420–440 nm and 510–535 nm. These PL peaks, specifically located at approximately 436.1 nm and 535 nm, correspond to the π–π* transition and π* → Polaron transition, respectively.[104,110] In rGO, a significant broad peak appears within the wavelength range of 400–450 nm, signifying the formation of additional sp^2 carbon atoms resulting from the reduction of GO. Moreover, a broad peak is observed in the range of 510–535 nm, suggesting a reduction in the quantity of disorder-induced states within the π–π* energy gap of rGO. This decrease in disorder-induced states contributes to the enrichment of small-sized sp^2 clusters in the rGO structure.[111] Moving forward to discuss PANI/rGO nanocomposites, the emission peaks predominantly originate from the π–π* transition of the benzenoid unit, transitioning from the polaronic band to the π band structures of PANI. This emission also signifies the presence of electronic states involved in the photoexcitation process. The arrangement of quinoid and benzenoid units in PANI facilitates the formation of singlet excitons, which subsequently undergo photonic emission as they decay to the ground state. Consequently, excitons significantly contribute in the photoluminescence behavior of conjugated polymers. This effect primarily stems from the inherent structure of the conjugated systems, where the delocalization of π-electrons facilitates more efficient charge carrier movement.[56] In PANI/rGO nanocomposites, the interaction between PANI and rGO creates an environment conducive to increased carrier mobility. The conjugation within PANI allows for a smoother transition of charge carriers, enhancing the overall electrical conductivity of the composite. This enhancement is particularly significant when considering the separation between electrons (e^-) and holes (h^+), which directly impacts the mobility of excitons (electron–hole pairs). The presence of rGO in the composite also plays a pivotal role. rGO, with its high surface area and

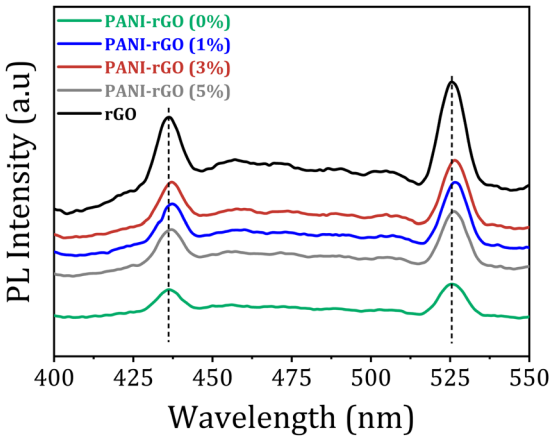

Fig. 8 PL spectrum of PANI, rGO, and PANI/rGO nanocomposites.

© 2024 The Author(s). Published by the Royal Society of Chemistry

Open Access Article. Published on 22 August 2024. Downloaded on 7/19/2025 1:42:39 AM. This article is licensed under a Creative Commons Attribution-NonCommercial 3.0 Unported Licence.

conductive nature, provides additional pathways for charge transfer, further augmenting the mobility of charge carriers within the composite material. This enhancement in excitons significantly contributes to a more pronounced PL. Interestingly, the PL intensity shows a remarkable amplification with the incorporation of rGO up to a specific threshold (3 wt%), beyond which a slight reduction is observed. This observation could be attributed due to improved charge transfer and reduced electron–hole recombination, excessive rGO can lead to the formation of non-radiative recombination centers, thus diminishing the PL intensity. The slight deviation in the emission peak in PANI/rGO nanocomposites is mainly influenced by variations in the arrangement of quinoid and benzenoid units within PANI.[105,112–114] As a result, these findings, in agreement with the UV-visible spectroscopy findings, afford compelling evidence of the substantial impact of rGO on the optical properties of PANI/rGO nanocomposites.

3.5.3. Raman spectroscopy. Raman spectroscopy serves as a rapid and nondestructive characterization method, providing valuable insights into the lattice structure, structural disorders, crystallization, and defects of carbon-based materials.[115] In this study, Raman analysis was utilized to explore the structural alterations in PANI throughout de-doping and re-doping procedures, as well as to analyze the vibrational spectrum of nonpolar bonds, particularly the C–C interactions within the PANI backbone and the basal planes of rGO. Fig. 9(A) presents the Raman spectra for rGO, PANI, and PANI/rGO (1, 3, and 5 wt%) nanocomposites.

The Raman spectra of rGO shows two discernible peaks with significance: one at 1351 cm^{-1} associated with the D mode, suggesting defects in graphitic carbon, and the other at 1580 cm^{-1} (G mode), aligning with the first-order scattering of the E_{2g} mode commonly observed in sp^2-carbon fields.[116,117] The extent of disorder in carbon materials is commonly assessed using the I_D/I_G ratio. In this case, the low I_D/I_G ratio of rGO (0.516) suggests a reduction in structural defects compared to its precursor material, GO. Literature reports suggest that the high I_D/I_G ratio in GO is indicative of a distorted lattice and a significant number of sp^3-like defects resulting from the oxidation process during its preparation.[118] The presence of oxygen-containing chemical moieties or groups during oxidation causes disturbances in the graphene lattice and leads to the formation of sp^3 carbon domains in GO. Nevertheless, during the reduction process, some of these defects are repaired, leading to a more ordered lattice in rGO defects by restoring the sp^2 hybridized carbon network and reducing the sp^3 domains, as evidenced by a lower I_D/I_G ratio. This process, however, might not completely eliminate all defects, leaving some residual disruptions in the lattice structure. The removal of oxygen-containing functional groups during reduction restores sp^2 carbon domains and recovers the graphene-like structure. As a consequence, the I_D/I_G ratio in rGO decreases, representing a reduction in the number of sp^3-like defects and an increase in the relative abundance of sp^2 carbon fields.[117,119]

The Raman spectrum of pristine PANI reveals distinct bands linked to the doped polymer, including C–H bending in the quinoid ring at 1161 cm^{-1}, C–N^+ stretching at 1329 cm^{-1}, and C═C stretching in the quinonoid ring at 1590 cm^{-1}. In PANI/rGO nanocomposites, the Raman spectra exhibits characteristic peaks consistent with those of pure PANI, corroborated by prior research, providing further evidence of the presence of PANI in the nanocomposites.[120–122] Interestingly, As the rGO content increases in the PANI/rGO nanocomposites, the vibration intensity at approximately 1470 cm^{-1} (corresponding to C═N quinoid stretching) undergoes changes, signifying that the addition of rGO encourages the prevalence of the quinoid form of PANI, promoting a conjugated planar arrangement. This finding is additionally substantiated by analyzing the intensity ratio of the C–H vibration in the quinoid unit (1150 cm^{-1}) relative to that of the consistent benzenoid (1160 cm^{-1}).[123,124] The stabilization of quinoid rings in the PANI/rGO nanocomposites is facilitated by π–π interactions with the basal planes of rGO, resulting in an increased level of polymer chain ordering within the hybrids.[119] This enhanced polymer chain ordering promotes stronger interactions and facilitates more effective charge transfer between rGO and PANI.

3.5.4. Fourier transformation infrared spectroscopy (FTIR). To complement the Raman data and gain insights into the interaction between rGO and PANI, FTIR spectroscopy was employed in this study. Fig. 9(B) showcases the FTIR spectra of PANI, rGO, as well as PANI/rGO nanocomposites (at 1, 3, and 5 wt% rGO) in the region between 1800 and 1000 cm^{-1}. This

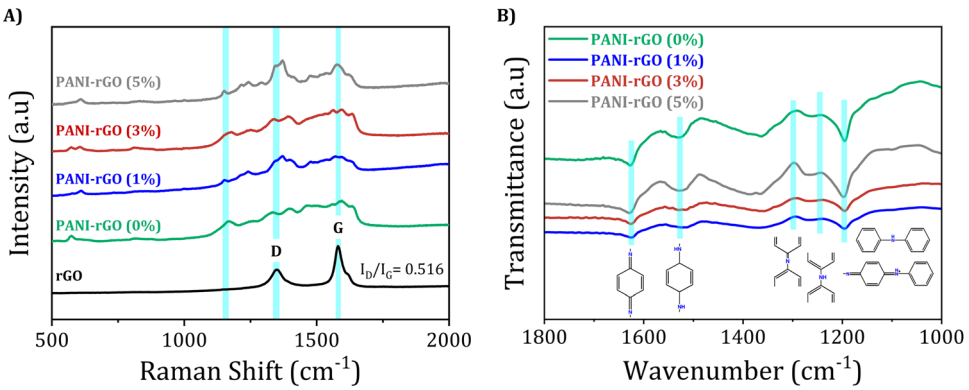

Fig. 9 (A) Raman spectra and (B) FT-IR spectrum of pure PANI, rGO, and PANI/rGO nanocomposites.

Open Access Article. Published on 22 August 2024. Downloaded on 7/19/2025 1:42:39 AM.
This article is licensed under a Creative Commons Attribution-NonCommercial 3.0 Unported Licence.

zoomed-in view allows for the identification of peaks resulting from the interactions between rGO and PANI. For further reference, Fig. S1 and S2 in the ESI† display the FTIR spectra of rGO and pure PANI, respectively.

Remarkably, the FTIR spectrum of rGO exhibited distinct changes, with a novel peak emerging at 1565 cm^{-1}, attributed to sp^2 hybridized C=C, and the disappearance of the peak at 1050 cm^{-1}, indicative of epoxide groups. These observations proved the successful reduction of GO to rGO, aligning with similar FTIR spectra reported in the literature for rGO.[125] In the FTIR spectrum of PANI and PANI/rGO nanocomposites, prominent absorption peaks are observed at 3277, 1623, 1428, and 1318 cm^{-1}, corresponding to N–H, C=N, C=C, and C–N stretching, correspondingly.[126] Notably, the intensity ratio of the PANI bands (1623 and 1428 cm^{-1}) is indicative of the occurrence of reduced (benzenoid) and oxidized (quinoid) repeat units. These characteristic bands serve as compelling evidence for the presence of the emeraldine salt phase of PANI in the nanocomposites.[127] The emeraldine salt phase represents the conductive state of PANI, featuring alternating benzenoid and quinoid repeat units. This conductive state is crucial for optimizing the electrical properties of PANI/rGO nanocomposites. In the structure of polyaniline, the alternating arrangement of benzenoid and quinoid units plays a crucial role in defining its electrical properties. This structural configuration facilitates the delocalization of π electrons across the benzenoid units, which is essential for the intrinsic conductivity of the polymer. This delocalization contributes to the overall electronic structure of PANI, allowing for a certain degree of electron mobility within the polymer chain. Simultaneously, the presence of quinoid units introduces sites for potential charge transfer interactions. These interactions are not purely based on the delocalization of π electrons but involve hopping mechanisms, where charge carriers, such as polarons and bipolarons, move between localized states along the polymer chain. This charge transfer process is influenced by the degree of oxidation (doping) of PANI and is critical in applications where PANI undergoes redox reactions or interacts with other materials, such as graphene in composites. Therefore, the electrical conductivity in PANI is a result of a complex interplay between the delocalization of π electrons, predominantly within the benzenoid segments, and charge transfer mechanisms, facilitated by the quinoid structures and doping levels. This interplay enables PANI to exhibit a range of conductive behaviors, adapting to different environmental conditions and applications. As a result, the presence of the emeraldine salt phase enables the efficient flow of electrons, contributing to improved electrical conductivity and enhanced performance of the nanocomposites in various applications, including energy storage devices, sensors, and conductive coatings. Interestingly, the FTIR spectrum of PANI/rGO nanocomposites did not exhibit the functional groups present on the rGO. This finding indicated that the surface of rGO was effectively coated with PANI through precise interactions, such as π–π electron stacking and H- bonding among the amine group of PANI and the oxygen groups in rGO.[128,129] Notably, the polymerization process involving aniline in the presence of rGO follows a specific mechanism. Aniline undergoes oxidation, consequential in the construction of oxidized radicals. These radicals then undergo a reductive elimination of $2H^+$ to form an α,α-aniline dimer. Subsequently, these dimers can propagate to longer chain lengths through repeated oxidation and reaction with generated aniline radicals *via* oxidation.[130] These interactions not only ensure the uniform dispersion of rGO within the PANI matrix but also contribute significantly to the improved electrical properties and overall performance of the PANI/rGO nanocomposites.

3.5.5. X-ray diffraction analysis (XRD). The structures of the PANI/rGO nanocomposites were further elucidated through powder X-ray diffraction (XRD) analyses. These analyses were conducted to investigate the elemental composition, carbon bonding, morphology, and crystallinity of the nanocomposites.[131] Fig. 10 illustrates the XRD patterns of pure rGO and PANI, as well as PANI/rGO (1, 3, and 5 wt%) nanocomposites. The XRD measurements were conducted over an angular range of $10^\circ \leq 2\theta \leq 60^\circ$, utilizing a scanning rate of 6° min^{-1} with a step size of 0.02°. In the XRD analysis of PANI, small diffraction peaks were observed at 15.20°, 20.20°, and a distinct peak at 25.50°, corresponding to the (011), (020), and (200) Bragg's reflections, correspondingly. These peaks are indicative of the crystalline planes associated with the emeraldine salt state of PANI.[132] The XRD pattern of rGO displayed peaks at $2\theta = 26.51^\circ$ and 44.40°, representing the characteristic (002) and (100) peaks of graphite-like structures, respectively. The intensities of these peaks amplified as a result of the interaction between rGO and PANI chains in different proportions.[101]

Upon forming the PANI/rGO nanocomposites, new peaks surfaced, demonstrating a shift compared to the pristine rGO peaks. This shift is ascribed to the π–π bond stacking of the benzene rings in PANI with rGO. Particularly, the peak at $2\theta = 25.50^\circ$ in pure PANI shifted to 26.60° when PANI was blended with rGO, signifying a substantial interaction between rGO particles and PANI chains.[21] Moreover, the XRD analysis of rGO/PANI nanocomposites revealed diffraction peaks similar to

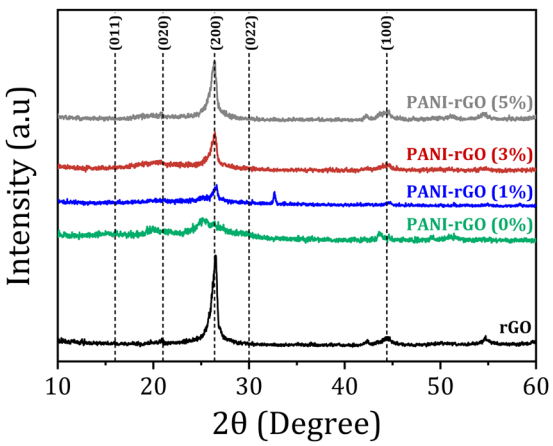

Fig. 10 XRD patterns of pure PANI, rGO, and PANI/rGO nanocomposites.

© 2024 The Author(s). Published by the Royal Society of Chemistry

Open Access Article. Published on 22 August 2024. Downloaded on 7/19/2025 1:42:39 AM. This article is licensed under a Creative Commons Attribution-NonCommercial 3.0 Unported Licence.

those observed in PANI or rGO, suggesting the absence of additional crystalline structures in the nanocomposite samples. Based on these outcomes, it can be resolved that the characteristic diffraction peaks indicate extensive physical and chemical interactions between rGO and PANI chains. These interactions include H-bonds, electrostatics, and π–π coordination interactions.[101]

3.6. X-ray photoelectron spectroscopy (XPS)

The investigation of elemental composition was advanced by X-ray photoelectron spectroscopy (XPS), providing deeper insights into the samples. The comprehensive survey spectra, as depicted in Fig. 11(A), distinctively portray the characteristic chemical profiles of pure PANI, rGO, and PANI/rGO nanocomposite samples, featuring discernible signals consistent to carbon (C 1s), nitrogen (N 1s), and oxygen (O 1s) for each respective material. Additionally, it is noteworthy that besides the detection of C KLL and O KLL Auger electron emissions in the high binding energy region, the oxygen signal present in the PANI sample may have arisen from residual APS as well as water molecules adsorbed onto the surface.[133] This oxygen signal might also stem from the rGO component within the PANI/rGO samples. Intriguingly, a subtle yet noteworthy N 1s peak observed in the rGO spectrum can be ascribed to doped nitrogen resulting from the hydrazine reduction process, thus further enriching our understanding of these intricate materials.[61,134]

Meanwhile, the N1s spectrum at high resolution for both PANI and PANI/rGO reveals four discernible components, as illustrated in Fig. 11(B) and (C). The peaks at binding energies of 398.1 and 399.2 eV are indicative of imine (–N═) and amine (–NH–) groups, respectively, while those at 401.6 and 405.1 eV are associated with positively charged nitrogen groups N^+ and $–NH^+$, respectively. PANI is predominantly composed of amine groups, suggesting its protoemeraldine form.[135,136] Throughout synthesis, PANI undergoes oxidation, leading to the partial conversion of amine to imine nitrogen. This transformation is explicable by the simultaneous reduction of GO oxygen functionalities and PANI nitrogen groups, facilitated by superheated water and the hydrothermal process,[137] also *via* hydrothermal process.[133] The heightened fraction of positively charged nitrogen can be attributed to the interactions between PANI and rGO, inducing a restructuring of the benzenoid amine structure of PANI. Moreover, the elevated doping level of PANI in this composite is expected to augment its electrical and electrochemical performance. The C 1s spectra' deconvolution for PANI, PANI/rGO nanocomposite, and rGO samples is presented in Fig. 11(D–F). Upon closer examination of the primary peak line of PANI, as shown in Fig. 11(D), a decomposition into four distinct peak lines becomes evident. Specifically, PANI displays a peak at 284.6 eV attributed to C–C and C═C bonds. Furthermore, characteristic peaks associated with carbon-nitrogen interactions manifest as follows: C–N, $C–N^+$, C═N, and C═O, each corresponding to binding energies of approximately 285.6, 286.7, as well as 287.9 eV, respectively. The presence of carbonyl functional groups within PANI can be ascribed to the generation of benzoquinone and hydroquinone, resulting from partial surface oxidation.[138] Turning attention to Fig. 11 (E and F), the C 1s spectrum for PANI/rGO and rGO display six discernible peak lines: C═C and C–C (284.31 eV), C–N (285.4 eV), C–OH (285.7 eV), C–O–C (286.6 eV), C═O bonds (288.1 eV), and π–π stacking (290.4 eV).[134,139] Notably, the C–N peaks are more prominent in the PANI/rGO spectra than in the rGO sample. While inherent oxygen defects may exist in the raw

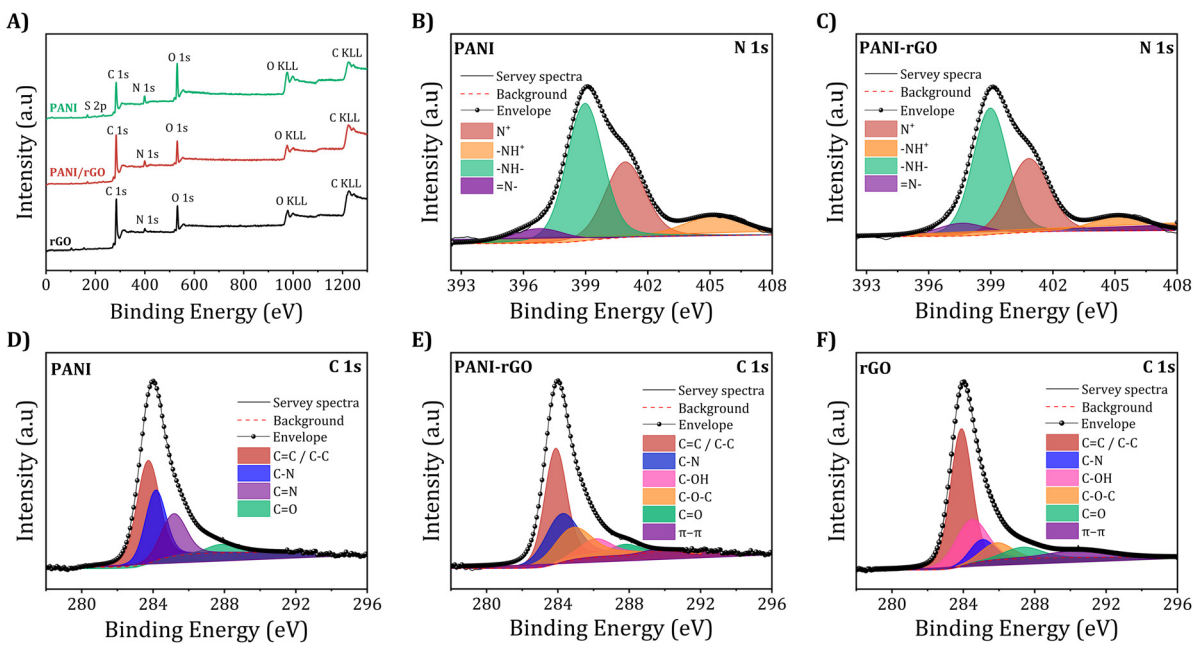

Fig. 11 XPS surveys with (A) the broad high-resolution spectrum of the (B and C) N 1s and (D–F) C 1s areas for pure PANI, rGO, and PANI/rGO nanocomposites (3 wt%).

Open Access Article. Published on 22 August 2024. Downloaded on 7/19/2025 1:42:39 AM.
This article is licensed under a Creative Commons Attribution-NonCommercial 3.0 Unported Licence.

rGO sample, the majority of the oxygen in the PANI/rGO nanocomposite coating likely originates from slight rGO oxidation during synthesis. This oxygen content acts as active sites, facilitating PANI polymerization. In this context, it is reasonable to infer that rGO contributes to the formation of a more comprehensive and densely structured PANI/rGO nanocomposite coating. This observation holds significant implications for the structural and functional properties of the resultant nanocomposite material.

3.7. Electrochemical behavior of PANI/rGO nanocomposites

To comprehend the electrochemical redox behavior of PANI/rGO nanocomposites, a conventional cyclic voltammetry (CV) test was performed. Fig. 12 illustrates the cyclic voltammograms of rGO, pure PANI, and PANI/rGO nanocomposites. When scanned at a rate of 25 mV s^{-1}, the CV of pure PANI exhibited the existence of two sets of redox peaks. These peaks correspond to specific transitions within the PANI structure, notably the shift from the fully-reduced PANI form (leucoemeraldine) to the partially-oxidized PANI form (emeraldine), as well as the transition among emeraldine and the fully-oxidized PANI form (pernigraniline).[1,35,122]

In contrast, the CV of PANI exhibits a single pair of redox peaks when scanned at rates ranging across 25 to 175 mV s^{-1}. It is important to note that as the scan rate rises from 25 to 175 mV s^{-1}, there is a proportional increase in current density. This increase can be ascribed to the interior resistance within the electrode. CV curves for PANI/rGO nanocomposites share a similar overall shape to that of pure PANI, but there is a noticeable difference in current densities. Specifically, the current densities of PANI/rGO nanocomposite samples are somewhat lower compared to PANI at equivalent potential scan

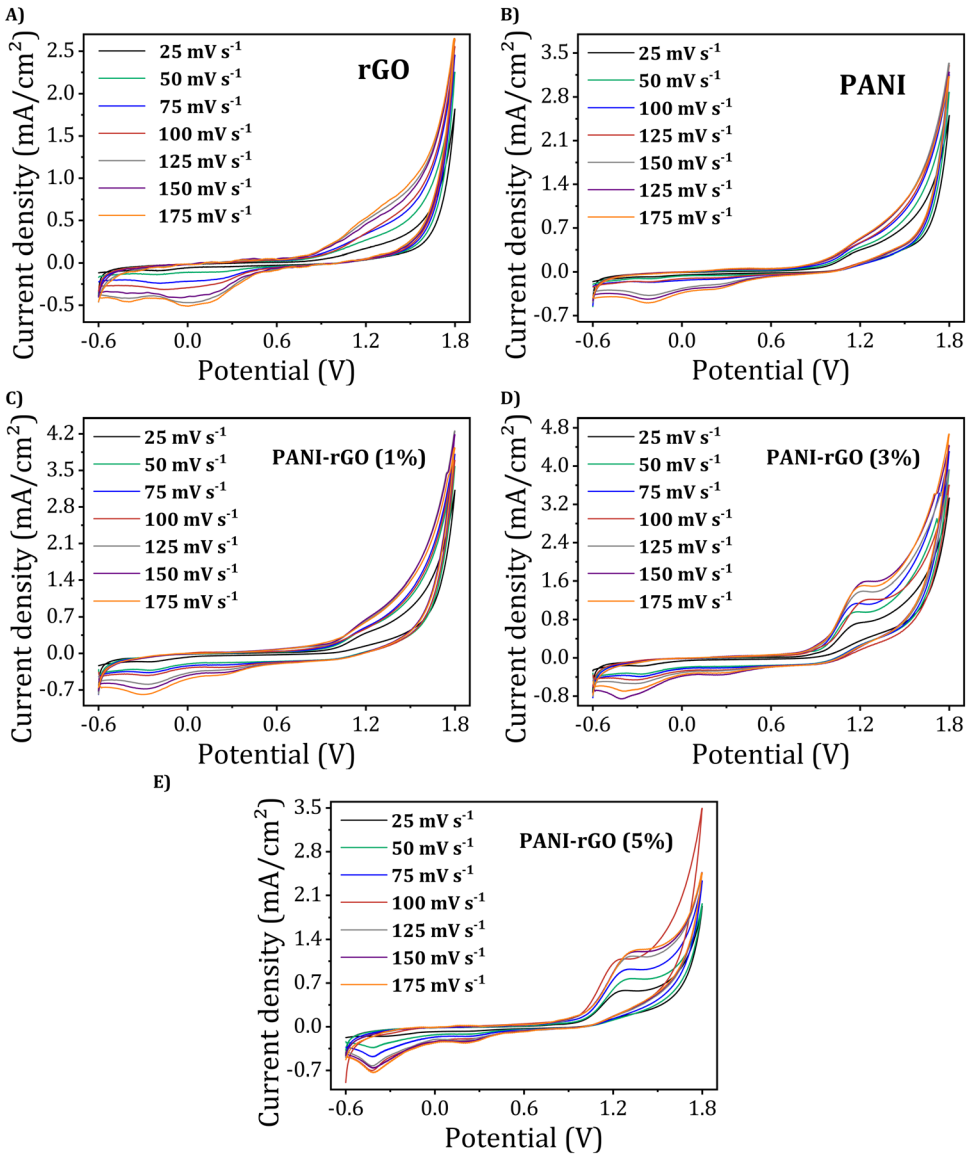

Fig. 12 Cyclic voltammograms of (A) rGO, (B) PANI, and PANI/rGO nanocomposites (C)–(E) at different scan rates.

© 2024 The Author(s). Published by the Royal Society of Chemistry

Open Access Article. Published on 22 August 2024. Downloaded on 7/19/2025 1:42:39 AM. This article is licensed under a Creative Commons Attribution-NonCommercial 3.0 Unported Licence.

rates. Moreover, by altering the weight percentage (wt%) of rGO in the PANI/rGO nanocomposites, significant changes in the profiles of the CV curves and current densities were observed. An increase in the rGO wt% from 3 wt% resulted in a substantial rise in current density. However, this trend was reversed as the rGO content was further increased to 5 wt%.

Using the CV data, the specific capacitances (C_p, F g^{-1}) were calculated for various potential scan rates (ν, mV s^{-1}) through the application of the following formula:

$$\text{Specific capacitance } (C_p) = \frac{\int I(V) \times dV}{m \times \Delta V \times \nu} \quad (12)$$

Here, $\int^{I}(V) \times dV$ signifies the integration of current over time, as acquired from the cyclic voltammogram, m denotes the mass of the sample, which, in this case, corresponds to the PANI/rGO nanocomposites, and is expressed in grams. ΔV represents the potential window, while ν represents the scan rate.

Fig. 13 offers an insightful evaluation by comparing the CV curves at a scan rate of 25 mV s^{-1} and the computed specific capacitances of pure PANI, rGO, and PANI/rGO nanocomposites. Notably, the trends in current density at 25 mV s^{-1} (Fig. 13(A)) and the specific capacitance (Fig. 13(B), as detailed in Table 5) align consistently. The order is as follows: PANI/rGO (3 wt%) < PANI/rGO (1 wt%) < PANI < PANI/rGO (5 wt%) < rGO. At a scan rate of 25 mV s^{-1}, the PANI/rGO (3 wt%) nanocomposite exhibits the highest specific capacitance, reaching a remarkable 145.79 F g^{-1}. The exceptional electrochemical behavior of PANI/rGO (3 wt%) can be attributed to an optimal balance between the conductive network provided by rGO and the electroactive surface area of PANI. An increase in the rGO content from 1 wt% to 3 wt% enhances the conductive pathways within the nanocomposite, thereby facilitating better charge transport and higher current densities. However, as the rGO content is further increased to 5 wt%, a decline in performance is observed. The decrease in current density and specific capacitance at 5 wt% rGO can be explained by the physics of percolation theory and the agglomeration effect.[65,140] While a moderate amount of rGO improves conductivity, excessive rGO leads to particle agglomeration. This agglomeration reduces the effective surface area and hinders the uniform dispersion of rGO within the PANI matrix. Consequently, the electrochemical active sites are less accessible, and the charge transfer resistance increases.[141] This phenomenon results in a decline in the overall electrochemical performance of the nanocomposite.

Table 5 Specific capacities of pure PANI, rGO, and PANI/rGO at a scan rate of 25 mV s^{-1}

Sample	Specific capacitance (F g^{-1})
PANI	101.87
PANI/rGO (1 wt%)	128.80
PANI/rGO (3 wt%)	145.79
PANI/rGO (5 wt%)	109.36
rGO	70.13

Thus, the finding that PANI/rGO (3 wt%) exhibits the highest specific capacitance underscores its exceptional electrochemical behavior, holding great promise for diverse sensor and energy storage applications.

3.8. Thermo-gravimetric analysis (TGA)

Thermogravimetry analysis (TGA) proves instrumental in discerning dopants and water content within polymers, offering valuable insights into thermal degradation patterns, structural characteristics, and thermal stability.[142] The progressive degradation at each step of the curve can be delineated through the mass loss profile. Employing TGA, we investigated the thermal stability of rGO, PANI, and PANI/rGO from room temperature up to 1000 °C (Fig. 14).

In the case of rGO, a significantly lower weight loss of approximately 11% was noted at 600 °C, demonstrating its heightened stability. The consistent weight reduction observed throughout the temperature spectrum emphasizes the enduring stability of rGO. The initial weight decline in rGO (~2%) below 100 °C is ascribed to the evaporation of adsorbed solvent molecules. Subsequently, a minor weight loss of ~5% and ~7% was observed in rGO between 100–300 °C and >300 °C, correspondingly. The gradual loss at temperatures exceeding 300 °C is linked to the elimination of more stable oxides,

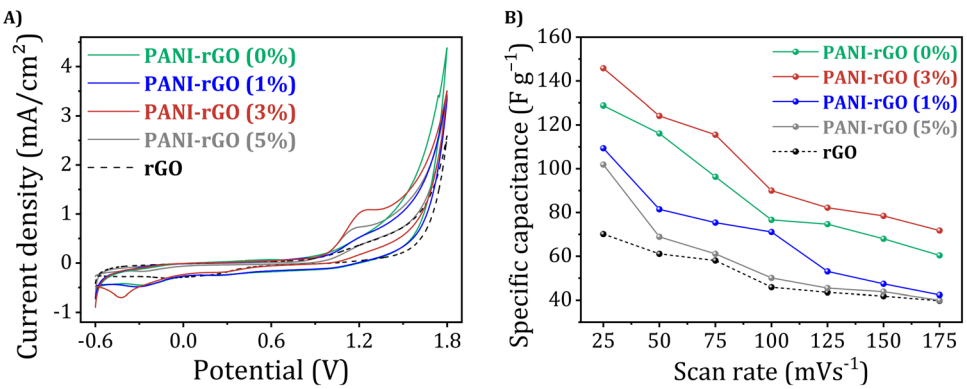

Fig. 13 (A) CV curves at a scan rate of 25 mV s^{-1} and (B) the computed specific capacitance of rGO, pure PANI, and rGO/PANI nanocomposites across various scan rate.

Open Access Article. Published on 22 August 2024. Downloaded on 7/19/2025 1:42:39 AM.
This article is licensed under a Creative Commons Attribution-NonCommercial 3.0 Unported Licence.

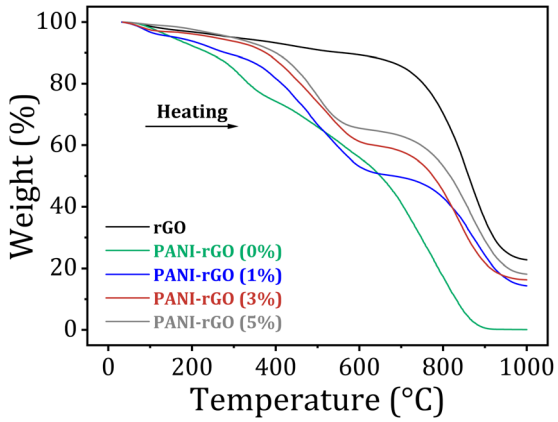

Fig. 14 The TGA profiles of pure PANI, rGO, and PANI/rGO nanocomposites.

particularly –COOH groups, with the partial presence of oxides validating the successful preparation of rGO.[143]

In PANI, a weight loss approximately 260 °C links to the evaporation of moisture content and dopants, initiating the breakdown of the PANI backbone beyond 260 °C.[144] PANI/rGO experiences rapid mass loss at approximately 390 °C, attributed to the decomposition of oxygen-containing groups such as –OH, –CO–, and –COOH.[145] Furthermore, Fig. 14 depicts that the thermal stability of the nanocomposite is shifted towards elevated temperatures in contrast to pure PANI. While PANI experiences complete decomposition at 767 °C, PANI/rGO nanocomposites exhibit decomposition temperatures of 838, 870, and 878 °C for PANI/rGO at 1%, 3%, and 5% *wt.*, respectively. This enhanced thermal stability can be attributed to the covalent bonding among rGO and the PANI backbone.[146] Moreover, these covalent bonds foster a substantial π–π stacking force amongst the basal plane of rGO and the PANI backbone, further reinforcing the nanocomposite's thermal stability.[147]

3.9. Computational calculations

In the pursuit of advancing materials science and engineering, the choice of appropriate models for the constituents of a nanocomposite material is paramount. In this study, a specific model for PANI and a distinct model for rGO were selected to comprehensively investigate the PANI–rGO nanocomposite. The overarching aim of this study is to align computational results with experimental findings. By selecting these tailored models for PANI and rGO, we aim to compare and confirm our computational outcomes with experimental data, reinforcing the credibility and applicability of our calculations. This holistic approach bridges the gap between theory and practice, fostering a deeper understanding of the PANI–rGO nanocomposite's structural and electronic properties, with significant implications for materials design and engineering applications.

3.9.1. Frontier molecular orbital (FMO) analysis. An advanced computational approach was utilized to explore the complex interaction configurations and electronic characteristics of PANI/rGO nanocomposites. Through FMO analysis, the most favorable interaction geometries were identified, offering valuable insights into the electronic properties of the nanocomposite system.

This analysis was conducted under several key assumptions that are essential for the computational modeling process. First, it was assumed that the molecular orbitals of the PANI, rGO, and PANI/rGO systems could be accurately represented as linear combinations of atomic orbitals (LCAO).[148] This is a well-established method in quantum chemistry, designed to simplify the intricate interactions within molecules. Additionally, the molecules were modeled as isolated entities in a vacuum environment, an approach that excludes solvent effects and other intermolecular interactions. While this assumption simplifies the computational process, it must be carefully considered when interpreting the results in practical, real-world contexts.[149,150] Moreover, the FMO analysis was based on the assumption that the molecules are in their ground state, focusing on their lowest energy configuration without considering possible excitations or the influence of external perturbations such as temperature variations or electromagnetic fields.[149,151] Lastly, electron correlation effects were approximated rather than fully incorporated, a common practice in DFT to ensure computational tractability, although this may lead to minor deviations in the calculated absolute energy levels.[152]

The optimized structures of PANI, rGO, and PANI/rGO, as depicted in Fig. 15 reveal a pronounced tendency of rGO to establish close interactions with the nitrogen (N) atoms of PANI. This is clearly illustrated in Fig. 15(C), where the intimate contact between rGO and the N atoms of PANI is distinctly observed. These interactions are crucial for understanding the electronic and molecular characteristics of the PANI/rGO nanocomposite, which may significantly influence its performance in various applications. These critical findings, illustrated in Fig. 15, provide invaluable insights into the optimized geometry of both PANI, rGO and the PANI/rGO nanocomposite. The interaction among rGO and PANI, as elucidated in the optimized structure, assumes paramount importance in comprehending the electronic and molecular characteristics of this nanocomposite material. To evaluate the comparative stability

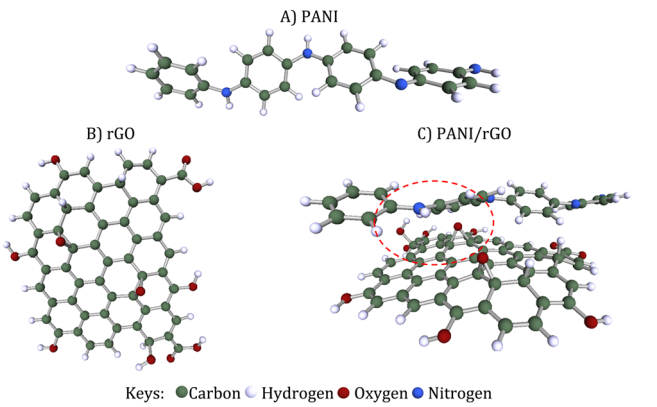

Fig. 15 Optimized geometry for (A) PANI, (B) rGO sheet, and (C) PANI–rGO nanocomposite.

© 2024 The Author(s). Published by the Royal Society of Chemistry

Open Access Article. Published on 22 August 2024. Downloaded on 7/19/2025 1:42:39 AM. This article is licensed under a Creative Commons Attribution-NonCommercial 3.0 Unported Licence.

and reactivity of the optimized structures, a range of parameters were systematically computed. These parameters include the interaction energy, energies of the E_{HOMO}, E_{LUMO}, and E_g.

The interaction energy was calculated by subtracting the sum of the electronic energies of the individual components (PANI and rGO) from the electronic energy of the resulting complex (PANI/rGO). The resulting negative interaction energy, in this case −12.566 eV, indicates that the formation of the PANI/rGO nanocomposite is exothermic. From a thermodynamic perspective, a negative interaction energy suggests that energy is released during the formation of the nanocomposite, which directly implies that the process is thermodynamically favorable. This exothermic reaction lowers the overall energy of the system, driving the formation of the complex.[72,153–155] The release of energy during bond formation between PANI and rGO signifies the creation of a more stable, lower-energy configuration compared to the isolated components. Hence, the negative interaction energy not only confirms the spontaneity of the complex formation but also reflects the strong interactions at the molecular level, which contribute to the enhanced stability and unique properties of the PANI/rGO nanocomposite.

Fig. 16 provides a comprehensive overview of the EHOMO and ELUMO, along with the energy gap, for the PANI, rGO, and PANI–rGO structures, all meticulously optimized in their most stable forms. The energy gap of a molecular structure is widely acknowledged as a crucial indicator of its electron transport properties.[44,156,157] Specifically, a lower energy gap in molecular structures suggests enhanced ease of electron transport. As illustrated in Fig. 16, the optimized configurations of PANI, rGO, and PANI–rGO exhibit energy gaps of 0.96 eV, 1.36 eV, and 2.15 eV, respectively. This observation aligns seamlessly with the experimental findings outlined in Section 3.5.1. This insight further underscores the potential of the PANI/rGO nanocomposite in facilitating efficient electron transport, a key attribute in various electronic applications.

3.9.2. COSMO-RS approach. Unveiling the structure–property relationship within molecular structures stands as a primary objective of COSMO-RS.[80,158–160] COSMO-RS, an advanced computational technique, utilizes quantum chemical computations and statistical thermodynamics to anticipate the thermodynamic attributes of both individual substances and their combinations.[75,77,161] It relies solely on details about the atoms in pure compounds, encompassing their geometry and charge shielding density, rendering it independent of experimental data.[162,163] The COSMO-RS charge distribution in the interacting system of PANI, rGO, and PANI–rGO is visually depicted on the COSMO surfaces, as illustrated in Fig. 17. Here, non-polar areas are represented in green, the acceptor of the hydrogen bond (HBA) location is shown in red, and the hydrogen bond donor is signified by the blue (HBD) region.[78,81,164]

In chemistry, sigma profiles and sigma potentials (σ-profiles and σ-potentials, respectively) are fundamental tools for studying the distribution of electrostatic potential around molecules and ions. They are pivotal in characterizing a molecule's electronic structure and chemical properties, aiding in predicting reactivity, stability, and other key attributes.[165,166] Within the COSMO-RS methodology, σ-profiles ($P(\sigma)$) offer graphical representations of charge shielding density on a molecular

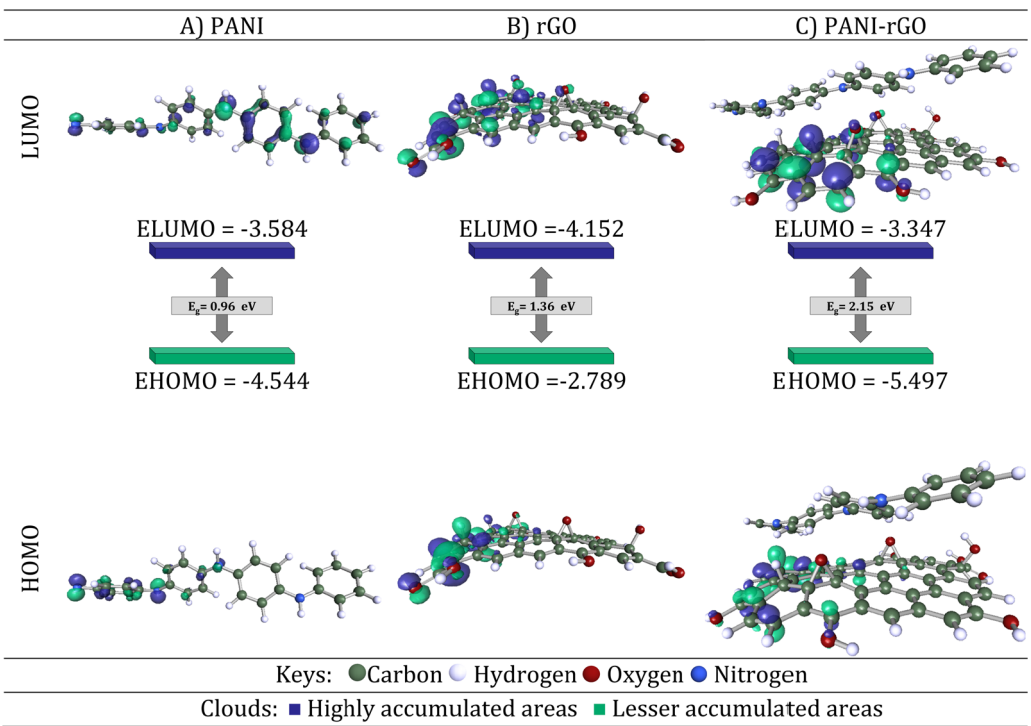

Fig. 16 Frontier molecular orbitals of (A) PANI, (B) rGO and (C) PANI–rGO nanocomposite.

Open Access Article. Published on 22 August 2024. Downloaded on 7/19/2025 1:42:39 AM.
This article is licensed under a Creative Commons Attribution-NonCommercial 3.0 Unported Licence.

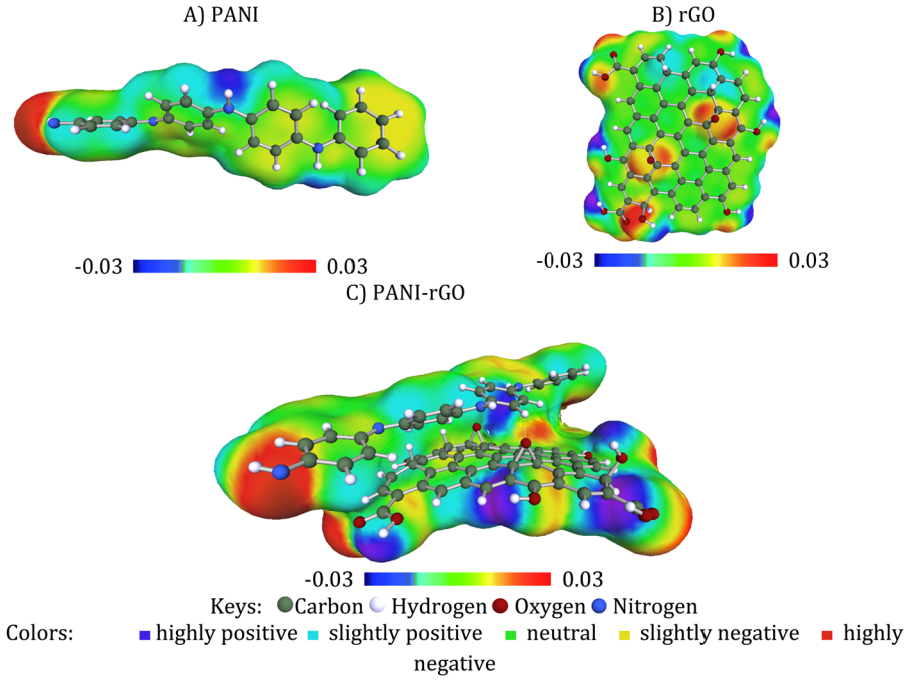

Fig. 17 Optimized COSMO-RS 3D structures of (A) PANI, (B) rGO, and (C) PANI–rGO models.

surface, providing insights into specific charge shielding densities in different regions. σ-Potentials ($\mu(\sigma)$), on the other hand, measure a molecule's interaction affinity by assessing the electrostatic potential energy at an exact point within the molecule, considering the surrounding solvent environment.[78,82,83] This metric helps evaluate the tendency of components in a mixture to interact with polar surfaces and establish hydrogen bonds. The electron density distribution is categorized into three regions: the HBD area ($\sigma < -0.0082$ e Å^{-2}), the non-polar area (-0.0082 e Å$^{-2} < \sigma < 0.0082$ e Å^{-2}), and the HBA area ($\sigma > 0.0082$ e Å^{-2}). Positive $\mu(\sigma)$ values indicate a higher occurrence of repulsive interactions, while negative values indicate more significant interactions among molecules.[167] The horizontal axis, with increasing positive and negative values representing H-bond thresholds, delineates areas within a molecule where HBDs interact with HBAs.[168]

In this investigation, Fig. 18 provides a compelling visualization of the σ-profiles as well as σ-potentials for both PANI and rGO, which offer profound insights into their unique characteristics. Upon scrutiny of the σ-profiles, it becomes evident that the PANI structure and rGO sheets predominantly exhibit nonpolar attributes, with discernible regions exhibiting a propensity for HBA, notably linked to the oxygen atoms within the rGO structure. Within the $P(\sigma)$, the central sector corresponds to nonpolar or weakly polar segments of the molecules, whereas the right-hand side reveals strongly polar areas, suggesting potential involvement in hydrogen bonding (Fig. 18(a)). On the left-hand side, HBD regions emerge. Within the carbon-rich zones, nonpolar characteristics prevail, denoted by the green regions in the surface charge distribution representations, signifying areas predominantly associated with exposed carbon atom surfaces. Peaks positioned within the HBA regions

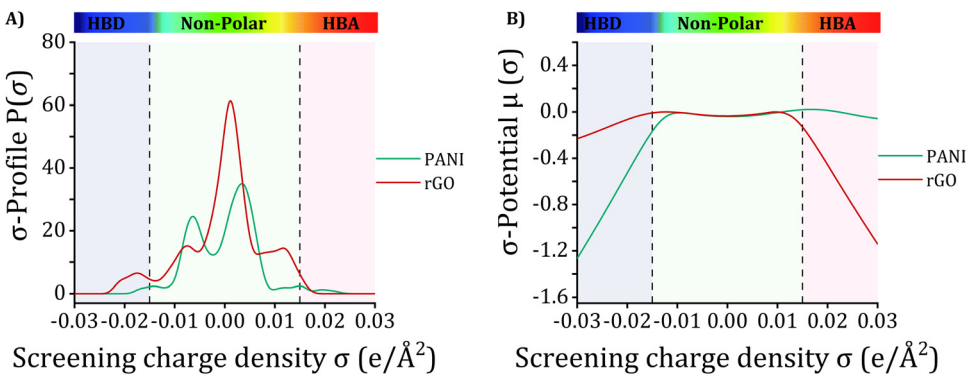

Fig. 18 (A) σ-Profiles and (B) σ-potentials derived by COSMO-RS for PANI and rGO models investigated in this study.

© 2024 The Author(s). Published by the Royal Society of Chemistry

Open Access Article. Published on 22 August 2024. Downloaded on 7/19/2025 1:42:39 AM.
This article is licensed under a Creative Commons Attribution-NonCommercial 3.0 Unported Licence.

link to the presence of oxygen atoms, depicted as red areas in the surface charge density; for rGO, this red area is correlated with the epoxy groups (as observed in Fig. 17(B)). In contrast, peaks within the HBS area of the σ-profile align with hydrogen atoms present in the alkyl side chains and hydroxyl groups, illustrated as light blue areas.[169] Moreover, a meticulous examination of the σ-potentials emphasizes that the primary interaction between PANI and rGO transpires within the polar region, encompassing both HBA and HBD sites. This phenomenon can be largely attributed to rGO's demonstrated capacity to establish hydrogen bonds, as indicated by positive $\mu(s)$ values.[153,170,171] Additionally, it is worth noting that viable interactions are not confined solely to the polar realm; they can also manifest within the nonpolar area, where rGO exhibits a negative $\mu(s)$ value (Fig. 18(b)).

This observation underscores the intricate nature of the interaction between PANI and rGO, which bridges both polar and nonpolar domains. Accordingly, the σ-profiles and σ-potentials of these distinct compounds provide appreciated insights into their chemical composition, accounting for polarization and their potential for hydrogen bonding. This comprehensive understanding significantly augments our

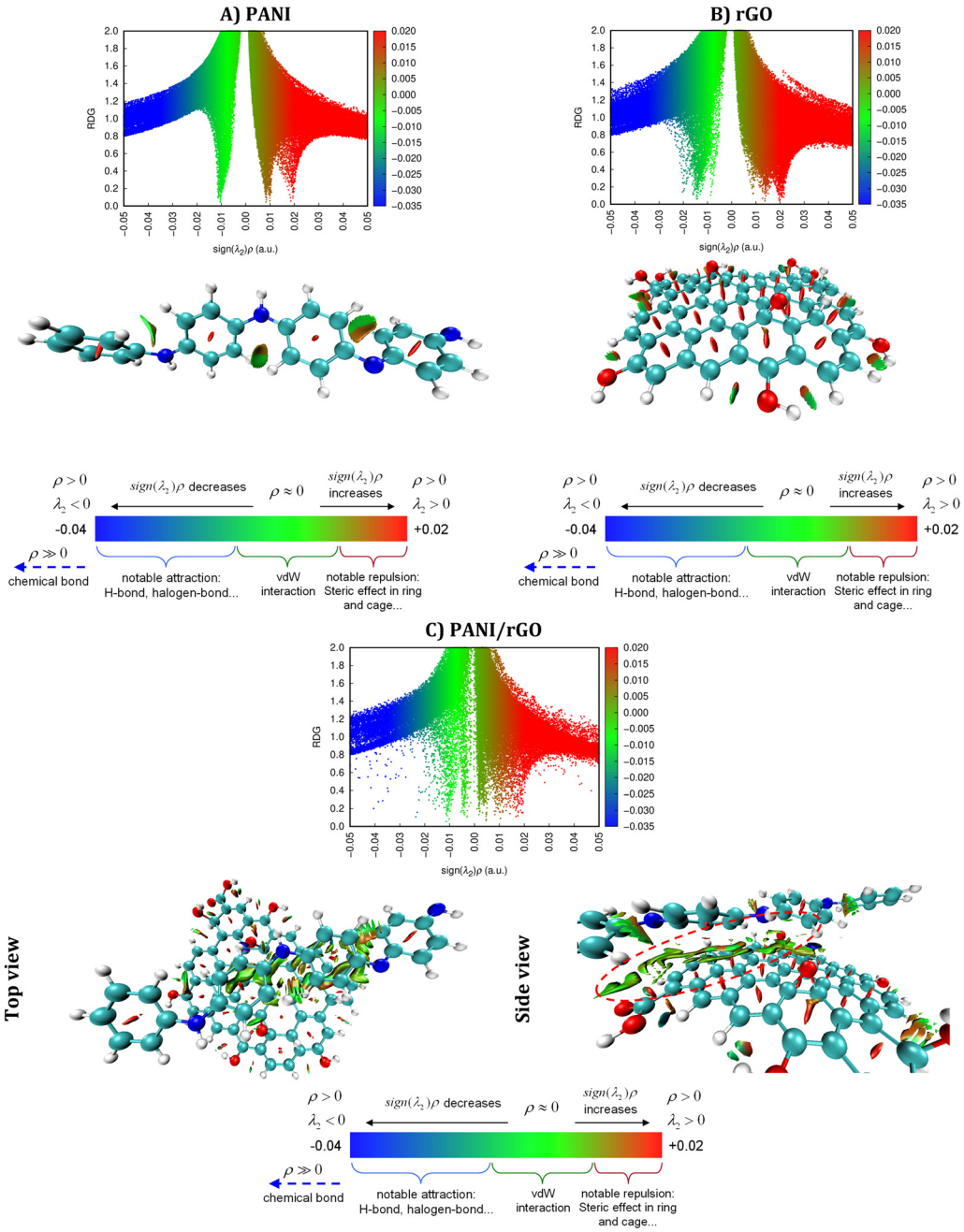

Fig. 19 Scatter plots for RDG (upper) and NCI (bottom) isosurfaces (s = 0.5 a.u.) of (A) PANI, (B) rGO, and (C) PANI/rGO isosurfaces (IGM = 0.01 a.u.). The isosurfaces' colors correspond to the sign values (λ_2) ρ, ranging from −0.05 to 0.05 a.u.

Open Access Article. Published on 22 August 2024. Downloaded on 7/19/2025 1:42:39 AM. This article is licensed under a Creative Commons Attribution-NonCommercial 3.0 Unported Licence.

understandings into the plausible interactions among the targeted PANI and rGO structures.

3.9.3. Non-covalent interaction (NCI) analysis. NCI analysis is an advanced theoretical method widely employed to elucidate intermolecular interactions and characterize weak forces within molecular systems.[172–174] This approach is particularly valuable for visualizing and quantifying the nature of these interactions through the use of ρ and the RDG, which are critical for identifying non-covalent interactions such as van der Waals forces, hydrogen bonding, and steric repulsions.

The capability of the NCI approach is measured by its ability to provide detailed insights into the strength, type, and distribution of these interactions across the molecular system. Specifically, NCI analysis employs the product of ρ and the sign of the second-highest eigenvalue λ_2 of the Hessian matrix of the electron density at each point on the isosurface. This product, $(\lambda_2) \times \rho$, is a key metric that allows for the differentiation between attractive and repulsive interactions. A negative value of $(\lambda_2) \times \rho$ indicates attractive forces, such as hydrogen bonds, while a positive value signifies repulsive interactions, like steric hindrances.[160,172,175]

The reliability and effectiveness of the NCI approach are gauged through its consistency with experimental observations and other computational methods. By accurately identifying and characterizing the non-covalent interactions that stabilize molecular structures, the NCI approach has been validated in numerous studies for its ability to predict interaction behavior that aligns well with empirical data. In this study, the capability of the NCI method was demonstrated by the clear identification of van der Waals forces as the predominant stabilizing interactions within the PANI/rGO nanocomposite, as shown in Fig. 19. The RDG isovalue range from −0.035 to 0.020 a.u., combined with the color-coded isosurfaces, effectively visualizes these interactions, further corroborating the stability of the nanocomposite.

For the PANI molecule, NCI analysis revealed intramolecular van der Waals forces, indicated by green surfaces in the 3D plot, with corresponding spikes at −0.01 a.u. in the 2D $s(\rho)$ plot. In the PANI/rGO system, a cluster of RDG spikes between 0.00 and −0.01 a.u. confirmed the presence of weak, yet significant, non-covalent interactions, primarily van der Waals forces, which contribute to the formation and stability of the nanocomposite. The application of the NCI approach in this study, therefore, demonstrates its robust capability in accurately mapping and quantifying the non-covalent interactions that underpin the structural integrity and functional properties of the PANI/rGO nanocomposite.

3.9.4. Quantum theory of atoms in molecules (QTAIM) results. The QTAIM framework is a well-established computational tool used for characterizing the strength and nature of interactions within chemical systems.[176–178] In Fig. 20, we present molecular graphs of the PANI/rGO system, which highlight the presence of bond critical points (BCPs) and bond paths. The identification of these BCPs confirms the transfer of electron density, substantiating the formation of chemical bonds between PANI and rGO.

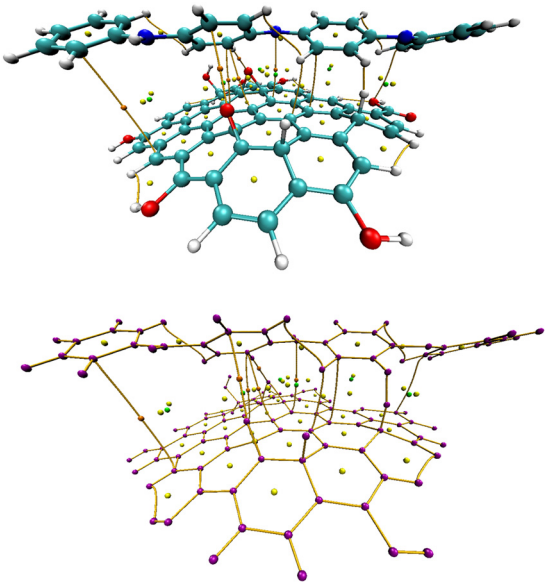

Fig. 20 QTAIM molecular graphs showing bond paths and critical points for PANI/rGO complex. Orange, yellow, and green dots signify BCP points, ring-critical points, and cage-critical points, correspondingly.

While specific benchmarking tests were not conducted as part of this study, it is important to note that the QTAIM methodology has been extensively validated and is widely recognized in the field of computational chemistry. The parameters we employed—such as electron density ($\rho(r)$), Laplacian of the electron density ($\Delta^2\rho(r)$), potential energy density ($V(r)$), Lagrangian kinetic energy ($G(r)$), and total energy density ($H(r)$)—are derived using well-established computational protocols. These protocols are widely accepted in the scientific literature and have been proven reliable for analyzing systems similar to the PANI/rGO nanocomposite.

In our study, BCPs were precisely identified by locating (3, −1) critical points (CPs), which are also known as saddle points, between interacting atoms or along the paths connecting analyte atoms to the surface.[75,179–181] These BCPs are critical in probing non-covalent interactions within two-fragment systems. The calculated parameters, detailed in Table 6, provide significant insights into the nature of the interactions within the PANI/rGO system.

The strength of intermolecular bonds between PANI and rGO was further investigated by classifying the interactions based on $\Delta^2\rho(r)$ and $H(r)$ values. Positive and negative values of these parameters correspond to weak and strong interactions, respectively. A negative $H(r)$ combined with a positive $\Delta^2\rho(r)$ indicates medium-strength interactions.[182] As shown in Table 6, $\rho(r)$ values with positive $\Delta^2\rho(r)$ are indicative of hydrogen bond interactions, as seen in the interaction between 125(H) and 88(O). Furthermore, the analysis revealed a strong tendency for rGO to interact closely with the nitrogen (N) atoms of PANI, evidenced by the BCP between 274 : 102(N) and 21(C). The ratio $|V(r)|V(r)$, which is less than 1, indicates that the electron's tendency to combine (represented by $V(r)$) is outweighed by their propensity to disperse (represented by $G(r)$).

© 2024 The Author(s). Published by the Royal Society of Chemistry

Open Access Article. Published on 22 August 2024. Downloaded on 7/19/2025 1:42:39 AM. This article is licensed under a Creative Commons Attribution-NonCommercial 3.0 Unported Licence.

Table 6 QTAIM characteristics of the interaction sites (in a.u.) at selected BCPs in PANI/rGO complex

BCP	X–Y	$\rho(r)$	$\Delta^2\rho(r)$	$V(r)$	$G(r)$	$\lvert V(r)\rvert/G(r)$	$H(r)$
164	91(C)–40(C)	0.000274	0.001532	−0.000132	0.000257	−0.511626	0.000126
175	54(O)–97(C)	0.005454	0.018768	−0.003213	0.003952	−0.812856	0.000740
247	100(C)–32(C)	0.004964	0.000702	−0.002328	0.003031	−0.768261	0.000702
248	100(C)–33(C)	0.004954	0.015022	−0.002333	0.003044	−0.766277	0.000711
274	102(N)–21(C)	0.004138	0.012777	−0.002290	0.002742	−0.835106	0.000452
284	125(H)–88(O)	0.041559	0.176644	−0.041626	0.042893	−0.970443	0.001268

This ratio suggests that the interactions between PANI and rGO are predominantly electrostatic in nature.[182] The application of well-established QTAIM methodologies, combined with adherence to rigorous computational protocols, ensures the robustness and reliability of our findings. Consequently, the insights gained into the bonding interactions within the PANI/rGO system provide valuable contributions to the advancement of nanocomposite technologies.

4. Conclusion

In the present work, we achieved the successful synthesis of PANI/rGO nanocomposites through an *in situ* chemical polymerization process facilitated by a deep eutectic solvent (DES) serving as an electrolyte. A thorough investigation was conducted, integrating response surface methodology (RSM), artificial neural networks (ANN), and molecular simulation techniques for the comprehensive modeling, optimization, and characterization of PANI/rGO nanocomposites. The collaborative implementation of optimization methods and meticulous characterization uncovered profound insights into the multifaceted characteristics of these nanocomposites. From this integrative approach, several key outcomes have emerged:

• RSM analysis elucidated the impact of APS/ANI molar ratio, rGO loading, and polymerization time on electrical conductivity, culminating in a second-order polynomial function. Optimal conditions for maximum electrical conductivity were identified as an APS/ANI molar ratio of 0.75, 3 wt% rGO loading, and a 6-hour polymerization time, yielding a high conductivity of 4.975×10^{-3} S cm^{-1}. ANN analysis exhibited enhanced conductivity of 4.988×10^{-3} S cm^{-1}, showcasing the superior predictive accuracy of the ANN model over RSM.

• Comprehensive characterization through UV-vis, PL, Raman, FTIR, and XRD elucidated significant structural changes in PANI/rGO nanocomposites, emphasizing the transformative impact of rGO on PANI.

• XPS analysis unveiled distinctive elemental compositions, with the deconvolution of C 1s spectra highlighting intensified C–N peaks in PANI/rGO, indicating a denser nanocomposite coating and promising structural enhancements.

• Electrochemical studies through cyclic voltammetry showcased superior capacitance in PANI/rGO, reaching an impressive 145.79 F g^{-1}, surpassing individual PANI or rGO components.

• TGA analysis affirmed the enhanced thermal stability of PANI/rGO, with decomposition temperatures notably higher than pure PANI, attributed to synergistic covalent bonding and substantial π–π stacking forces.

• Molecular-level insights through FMO, COSMO-RS, NCI, and QTAIM analyses provided a nuanced understanding of the PANI–rGO system, highlighting the dominant role of van der Waals forces in nanocomposite formation and stability.

To sum up, this study presents an innovative approach for fabricating multifunctional PANI/rGO nanocomposites, highlighting their potential in applications such as supercapacitors and gas sensors. These nanocomposites offer significant promise for advancing materials and promoting eco-friendly innovations. Future research should focus on the long-term stability and performance of PANI/rGO nanocomposites under various environmental conditions, scalable synthesis methods for industrial production, functionalization and doping to enhance specific properties, advanced characterization techniques for deeper insights, integrating PANI/rGO with other materials to develop hybrid systems, and conducting theoretical and computational studies to predict material behavior and design new composites. These efforts will pave the way for utilizing PANI/rGO nanocomposites in advanced energy storage devices, environmental sensors, and next-generation electronic materials.

However, several limitations need to be addressed for successful industrial application. Reproducibility at a larger scale is challenging due to variations in DES composition and the need for precise control over reaction conditions. Scaling up requires maintaining uniform temperature, mixing conditions, and reaction times. The use of specialized chemicals may increase costs and pose availability issues. While DES is more environmentally friendly than conventional solvents, its potential toxicity and environmental impact require thorough evaluation. The dual optimization strategy adds complexity, requiring specialized knowledge and resources. Additionally, the long-term stability of the nanocomposites under various environmental conditions needs further investigation.

This study presents a novel and superior method for synthesizing PANI/rGO nanocomposites, addressing gaps in existing literature and offering a comprehensive optimization strategy for enhanced electrical conductivity. Addressing these limitations is crucial for the successful industrial application of these promising materials.

Author contributions

Conceptualization and methodology (A. B., Z. G., N. H., M. B., Y. B.); validation (A. B., Z. G., N. H., M. B., I. L., I. B., O. M., S. I. A., M. A., Y. B.);

Open Access Article. Published on 22 August 2024. Downloaded on 7/19/2025 1:42:39 AM. This article is licensed under a Creative Commons Attribution-NonCommercial 3.0 Unported Licence.

formal analysis (A. B., I. L., I. B., O. M., S. I. A.); investigation (A. B., Z. G., N. H., M. B., O. M., Y. B.); resources (Y. B., M. A.); writing – original draft (A. B., Z. G., N. H., M. B., Y. B.); writing – review & editing (A. B., Z. G., N. H., M. B., I. L., I. B., O. M., S. I. A., M. A., Y. B.); visualization (A. B., Y. B.); supervision (Z. G., N. H., M. B., Y. B.); project administration (Z. G., N. H., M. B., M. A., Y. B.); funding acquisition (M. A.).

Data availability

The data supporting the findings of this study are available within the article and its ESI.†

Conflicts of interest

There are no conflicts to declare.

Acknowledgements

The authors are grateful for the support received from the Laboratory of Electrochemistry-Corrosion, Metallurgy and Inorganic Chemistry, Faculty of Chemistry, USTHB, BP 32 El-Alia,16111 Algiers, Algeria, the Ministry of Higher Education and Scientific Research, Ferhat ABBAS Setif 1 University, and the Directorate General for Scientific Research and Technological Development (DGRSDT), Algeria. The authors acknowledge the generous support of the researchers supporting project number (RSP-2024/R113), King Saud University, Riyadh, Saudi Arabia.

References

1 A. Boublia, Z. Guezzout, N. Haddaoui, M. Badawi, A. S. Darwish, T. Lemaoui, S. E. I. Lebouachera, K. K. Yadav, M. A. Alreshidi, J. S. Algethami, M. Abbas, F. Banat, I. M. AlNashef, B. H. Jeon and Y. Benguerba, *Crit. Rev. Solid State Mater. Sci.*, 2023, **0**, 1–25.
2 H. D. Kyomuhimbo and U. Feleni, *Electroanalysis*, 2023, **35**, e202100636.
3 T. Sen, S. Mishra and N. G. Shimpi, *RSC Adv.*, 2016, **6**, 42196–42222.
4 H. N. Heme, M. S. N. Alif, S. M. S. M. Rahat and S. B. Shuchi, *J. Energy Storage*, 2021, **42**, 103018.
5 X. Hong, J. Fu, Y. Liu, S. Li, X. Wang, W. Dong and S. Yang, *Materials*, 2019, **12**, 1451.
6 H. Chen, F. Zhuo, J. Zhou, Y. Liu, J. Zhang, S. Dong, X. Liu, A. Elmarakbi, H. Duan and Y. Fu, *Chem. Eng. J.*, 2023, **464**, 142576.
7 Y. Zhang, X. Chen, H. Chen, M. Jia, H. Cai, Z. Mao and Y. Bai, *Chem. Eng. J.*, 2023, **470**, 143912.
8 A. K. Geim and K. S. Novoselov, *Nanosci. Nanotechnol.*, 2009, **6**, 11–19.
9 Y. Zhu, S. Murali, W. Cai, X. Li, J. W. Suk, J. R. Potts and R. S. Ruoff, *Adv. Mater.*, 2010, **22**, 3906.
10 M. Sabet, H. Soleimani and S. Hosseini, *J. Vinyl Addit. Technol.*, 2018, **24**, E177–E185.
11 M. D. Stoller, S. Park, Y. Zhu, J. An and R. S. Ruoff, *Nano Lett.*, 2008, **8**, 3498–3502.
12 D. S. L. Abergel, V. Apalkov, J. Berashevich, K. Ziegler and T. Chakraborty, *Adv. Phys.*, 2010, **59**, 261–482.
13 N. A. Kumar and J. B. Baek, *Chem. Commun.*, 2014, **50**, 6298–6308.
14 K. S. Novoselov, *et al.*, *Science*, 2016, **306**, 666–669.
15 L. Wang, X. Lu, S. Lei and Y. Song, *J. Mater. Chem. A*, 2014, **2**, 4491–4509.
16 A. M. Díez-Pascual and J. A. Luceño-Sánchez, *Polymers*, 2021, **13**, 2105.
17 L. Chen, N. Li, X. Yu, S. Zhang, C. Liu, Y. Song, Z. Li, S. Han, W. Wang, P. Yang, N. Hong, S. Ali and Z. Wang, *Chem. Eng. J.*, 2023, **462**, 142139.
18 F. Kazemi, S. M. Naghib, Y. Zare and K. Y. Rhee, *Polym. Rev.*, 2021, **61**, 553–597.
19 A. Ladrón-de-Guevara, A. Boscá, J. Pedrós, E. Climent-Pascual, A. de Andrés, F. Calle and J. Martínez, *Appl. Surf. Sci.*, 2019, **467–468**, 691–697.
20 M. K. Ali, A. Hessein, M. A. Hassan, M. Ghali, N. M. Shaalan, K. Nakamura and A. A. El-Moneim, *J. Appl. Polym. Sci.*, 2021, **138**, 50852.
21 M. Mitra, C. Kulsi, K. Chatterjee, K. Kargupta, S. Ganguly, D. Banerjee and S. Goswami, *RSC Adv.*, 2015, **5**, 31039–31048.
22 V. H. N. Martins, N. M. S. Siqueira, J. E. S. Fonsaca, S. H. Domingues and V. H. R. Souza, *ACS Appl. Nano Mater.*, 2021, **4**, 5553–5563.
23 X. Huang, N. Hu, R. Gao, Y. Yu, Y. Wang, Z. Yang, E. Siu-Wai Kong, H. Wei and Y. Zhang, *J. Mater. Chem.*, 2012, **22**, 22488–22495.
24 J. Chang, X. Zhang, Z. Wang, C. Li, Q. Hu, J. Gao and L. Feng, *ACS Appl. Nano Mater.*, 2021, **4**, 5263–5272.
25 N. Zhao, Z. Ma, H. Song, D. Wang and Y. Xie, *Int. J. Hydrogen Energy*, 2018, **43**, 17867–17872.
26 N. P. S. Chauhan, M. Mozafari, N. S. Chundawat, K. Meghwal, R. Ameta and S. C. Ameta, *J. Ind. Eng. Chem.*, 2016, **36**, 13–29.
27 N. Gao, J. Yu, S. Chen, X. Xin and L. Zang, *Synth. Met.*, 2021, **273**, 116693.
28 N. Gospodinova and L. Terlemezyan, *Prog. Polym. Sci.*, 1998, **23**, 1443–1484.
29 G. Ciric-Marjanovic, *Synth. Met.*, 2013, **177**, 1–47.
30 A. Boublia, Z. Guezzout, N. Haddaoui, M. Badawi, A. S. Darwish, T. Lemaoui, F. Banat, K. K. Yadav, B. H. Jeon, N. Elboughdiri, Y. Benguerba and I. M. Al Nashef, *J. Mater. Chem. A*, 2023, **12**, 2209–2236.
31 A. L. Pang, A. Arsad and M. Ahmadipour, *Polym. Adv. Technol.*, 2021, **32**, 1428–1454.
32 S. Ameen, M. Shaheer Akhtar and M. Husain, *Sci. Adv. Mater.*, 2010, **2**, 441–462.
33 H. Sharifi, M. Zabihzadeh and M. Ghorbani, *Carbohydr. Polym.*, 2018, **194**, 384–394.
34 A. Boublia, S. E. I. Lebouachera, N. Haddaoui, Z. Guezzout, M. A. Ghriga, M. Hasanzadeh, Y. Benguerba and

© 2024 The Author(s). Published by the Royal Society of Chemistry

Open Access Article. Published on 22 August 2024. Downloaded on 7/19/2025 1:42:39 AM. This article is licensed under a Creative Commons Attribution-NonCommercial 3.0 Unported Licence.

N. Drouiche, *Polym. Bull.*, 2023, **80**, 5999–6031, DOI: 10.1007/s00289-022-04398-6.
35 C. H. B. Silva, M. Iliut, C. Muryn, C. Berger, Z. Coldrick, V. R. L. Constantino, M. L. A. Temperini and A. Vijayaraghavan, *Beilstein J. Nanotechnol.*, 2018, **9**, 2936–2946.
36 S. L. C. Ferreira, R. E. Bruns, H. S. Ferreira, G. D. Matos, J. M. David, G. C. Brandão, E. G. P. da Silva, L. A. Portugal, P. S. dos Reis, A. S. Souza and W. N. L. dos Santos, *Anal. Chim. Acta*, 2007, **597**, 179–186.
37 N. Szpisják-Gulyás, A. N. Al-Tayawi, Z. H. Horváth, Z. László, S. Kertész and C. Hodúr, *Acta Aliment.*, 2023, **52**, 521–537.
38 J. M. Zurada, *Data mining with computational intelligence*, Springer Science & Business Media, 2006, vol. 17.
39 I. M. Savic, D. G. Gajic and I. M. Savic-Gajic, *Artif. Neural Networks New Res.*, 2017, **17**, 1–24.
40 M. Abd Elaziz, A. Dahou, L. Abualigah, L. Yu, M. Alshinwan, A. M. Khasawneh and S. Lu, *Neural Comput. Appl.*, 2021, **33**, 14079–14099.
41 J. Neugebauer and T. Hickel, *Wiley Interdiscip. Rev. Comput. Mol. Sci.*, 2013, **3**, 438–448.
42 Y. Qiao, M. Luo, Q. Yin, Y. Wang and G. Zhou, *Macromol. Theory Simul.*, 2023, **32**, 2300023.
43 I. B. Obot, D. D. Macdonald and Z. M. Gasem, *Corros. Sci.*, 2015, **99**, 1–30.
44 B. A. Farooqi, M. Yar, A. Ashraf, U. Farooq and K. Ayub, *Eur. Polym. J.*, 2020, **138**, 109981.
45 X. Zheng, M. E. Ali Mohsin, A. Arsad and A. Hassan, *J. Appl. Polym. Sci.*, 2021, **138**, 50637.
46 E. J. Jelmy, S. Ramakrishnan, S. Devanathan, M. Rangarajan and N. K. Kothurkar, *J. Appl. Polym. Sci.*, 2013, **130**, 1047–1057.
47 M. Reza, N. Srikandi, A. N. Amalina, D. P. Benu, F. V. Steky, A. Rochliadi and V. Suendo, *IOP Conference Series: Materials Science and Engineering*, IOP Publishing, 2019, vol. 599, p. 12002.
48 H. Nazari and R. Arefinia, *Int. J. Polym. Anal. Charact.*, 2019, **24**, 178–190.
49 P. N. Adams, P. J. Laughlin, A. P. Monkman and A. M. Kenwright, *Polymer*, 1996, **37**, 3411–3417.
50 M. M. Rahman, T. Mahtab, M. Z. Bin Mukhlish, M. O. Faruk and M. M. Rahman, *Polym. Bull.*, 2021, **78**, 5379–5397.
51 Y. Cao, A. Andreatta, A. J. Heeger and P. Smith, *Polymer*, 1989, **30**, 2305–2311.
52 I. Sapurina and J. Stejskal, *Polym. Int.*, 2008, **57**, 1295–1325.
53 P. P. Sengupta and B. Adhikari, *Mater. Sci. Eng., A*, 2007, **459**, 278–285.
54 G. M. Neelgund and A. Oki, *Polym. Int.*, 2011, **60**, 1291–1295.
55 O. A. Al-Hartomy, S. Khasim, A. Roy and A. Pasha, *Appl. Phys. A: Mater. Sci. Process.*, 2019, **125**, 1–9.
56 V. G. Sreeja, G. Vinitha, R. Reshmi, M. K. Jayaraj and E. I. Anila, *Mater. Today Proc.*, 2019, **10**, 456–465.
57 F. Yilmaz and Z. Küçükyavuz, *E-Polymers*, 2009, **9**, 1–10.
58 A. M. Díez-Pascual, *Polymers*, 2021, **13**, 1–15.
59 Z. Guezzout, A. Boublia and N. Haddaoui, *J. Polym. Res.*, 2023, **30**, 1–16.
60 F. Usman, J. O. Dennis, K. C. Seong, A. Yousif Ahmed, F. Meriaudeau, O. B. Ayodele, A. R. Tobi, A. A. S. Rabih and A. Yar, *Results Phys.*, 2019, **15**, 102690.
61 V. H. Nguyen, C. Lamiel, D. Kharismadewi, V. C. Tran and J. J. Shim, *J. Electroanal. Chem.*, 2015, **758**, 148–155.
62 H. K. Ismail, H. F. Alesary and M. Q. Mohammed, *J. Polym. Res.*, 2019, **26**, 1–12.
63 M. Mitra, S. T. Ahamed, A. Ghosh, A. Mondal, K. Kargupta, S. Ganguly and D. Banerjee, *ACS Omega*, 2019, **4**, 1623–1635.
64 H. Habib, I. S. Wani and S. Husain, *J. Energy Storage*, 2022, **55**, 105732.
65 O. Okhay and A. Tkach, *Nanomaterials*, 2022, **12**, 2531.
66 K. Hornik, M. Stinchcombe and H. White, *Neural Networks*, 1989, **2**, 359–366.
67 M. Pirdashti, S. Curteanu, M. H. Kamangar, M. H. Hassim and M. A. Khatami, *Rev. Chem. Eng.*, 2013, **29**, 205–239.
68 A. Susaimanickam, P. Manickam and A. A. Joseph, *Arch. Comput. Methods Eng.*, 2023, **30**, 4831–4853.
69 U. Shankar, R. Gogoi, S. K. Sethi and A. Verma, *Lecture Notes in Applied and Computational Mechanics*, Springer, 2022, vol. 99, pp. 299–313.
70 D. Bousba, C. Sobhi, E. Zouaoui, K. Rouibah, A. Boublia, H. Ferkous, A. Haddad, A. Gouasmia, I. Avramova, Z. Mohammed, V. I. Parvulescu, K. K. Yadav, M. Hasan, M. M. S. Cabral-Pinto, N. Elboughdiri and Y. Benguerba, *Energy Convers. Manage.*, 2024, **300**, 118021.
71 T. Zhang, Q. Xue, S. Zhang and M. Dong, *Nano Today*, 2012, **7**, 180–200.
72 T. Yasmin, A. Mahmood, M. Farooq, U. Rehman, R. M. Sarfraz, H. Ijaz, M. R. Akram, A. Boublia, M. M. Salem Bekhit, B. Ernst and Y. Benguerba, *Int. J. Biol. Macromol.*, 2023, **253**, 127032.
73 K. A. Moltved and K. P. Kepp, *Chem. Phys. Chem.*, 2019, **20**, 3210–3220.
74 N. Ramdane, Z. Marsa, A. Delimi, A. Sedik, A. Boublia, G. S. Albakri, M. Abbas, K. Kumar Yadav, M. Gabsi, A. Djedouani, K. O. Rachedi, L. Toukal, H. Benzouid, M. Berredjem, H. Ferkous and Y. Benguerba, *Inorg. Chem. Commun.*, 2024, **165**, 112479.
75 Z. Jebali, H. Ferkous, M. Zerroug, A. Boublia, A. Delimi, A. Bouzid, H. Majdoub, B. Ernst, N. Elboughdiri and Y. Benguerba, *J. Environ. Chem. Eng.*, 2024, **12**, 112374.
76 T. Himeur, K. Rouibah, H. Ferkous, A. Boublia, K. O. Rachedi, K. Harouche, C. Boulechfar, A. Abdennouri and Y. Benguerba, *Process Saf. Environ. Prot.*, 2024, **187**, 1422–1445.
77 I. Kaabi, S. Amamra, T. Douadi, M. Al-Noaimi, N. Chafai, A. Boublia, M. Albrahim, N. Elboughdiri and Y. Benguerba, *J. Taiwan Inst. Chem. Eng.*, 2024, **161**, 105535.
78 A. Mouffok, D. Bellouche, I. Debbous, A. Anane, Y. Khoualdia, A. Boublia, A. S. Darwish, T. Lemaoui and Y. Benguerba, *J. Mol. Liq.*, 2023, **375**, 121321.
79 D. Uka, B. Blagojević, O. Alioui, A. Boublia, N. Elboughdiri, Y. Benguerba, T. Jurić and B. M. Popović, *J. Mol. Liq.*, 2023, **391**, 123411.

Open Access Article. Published on 22 August 2024. Downloaded on 7/19/2025 1:42:39 AM. This article is licensed under a Creative Commons Attribution-NonCommercial 3.0 Unported Licence.

80 A. Mouffok, A. Boublia, D. Bellouche, S. D. Zed, N. Tabhirt, M. Alam, B. Ernst and Y. Benguerba, *Int. J. Environ. Health Res.*, 2024, 1–22.
81 T. Lemaoui, A. Boublia, A. S. Darwish, M. Alam, S. Park, B. H. Jeon, F. Banat, Y. Benguerba and I. M. Alnashef, *ACS Omega*, 2022, **7**, 32194–32207.
82 A. Boublia, T. Lemaoui, J. AlYammahi, A. S. Darwish, A. Ahmad, M. Alam, F. Banat, Y. Benguerba and I. M. AlNashef, *ACS Sustain. Chem. Eng.*, 2023, **11**, 208–227.
83 A. Boublia, T. Lemaoui, F. Abu Hatab, A. S. Darwish, F. Banat, Y. Benguerba and I. M. AlNashef, *J. Mol. Liq.*, 2022, **366**, 120225.
84 T. Lemaoui, A. Boublia, S. Lemaoui, A. S. Darwish, B. Ernst, M. Alam, Y. Benguerba, F. Banat and I. M. AlNashef, *ACS Sustainable Chem. Eng.*, 2023, **11**, 9564–9580.
85 J. AlYammahi, A. S. Darwish, T. Lemaoui, A. Boublia, Y. Benguerba, I. M. AlNashef and F. Banat, *ACS Omega*, 2023, **8**, 26533–26547.
86 D. R. Dreyer, S. Park, C. W. Bielawski and R. S. Ruoff, *Chem. Soc. Rev.*, 2010, **39**, 228–240.
87 S. K. Saha, M. Murmu, N. C. Murmu and P. Banerjee, *J. Mol. Liq.*, 2022, **364**, 120033.
88 E. R. Johnson, S. Keinan, P. Mori-Sánchez, J. Contreras-García, A. J. Cohen and W. Yang, *J. Am. Chem. Soc.*, 2010, **132**, 6498–6506.
89 Y. Islam Touahria, N. Chafai, O. Moumeni, A. Boublia, M. Mehri and Y. Benguerba, *J. Mol. Liq.*, 2024, **403**, 124897.
90 S. Mandal, S. Bej and P. Banerjee, *J. Mol. Liq.*, 2023, **381**, 121789.
91 A. Boutouil, M. R. Laamari, I. Elazhary, L. Bahsis, H. Anane and S. E. Stiriba, *Mater. Chem. Phys.*, 2020, **241**, 122420.
92 S. G. Balasubramani, G. P. Chen, S. Coriani, M. Diedenhofen, M. S. Frank, Y. J. Franzke, F. Furche, R. Grotjahn, M. E. Harding, C. Hättig, A. Hellweg, B. Helmich-Paris, C. Holzer, U. Huniar, M. Kaupp, A. Marefat Khah, S. Karbalaei Khani, T. Müller, F. Mack, B. D. Nguyen, S. M. Parker, E. Perlt, D. Rappoport, K. Reiter, S. Roy, M. Rückert, G. Schmitz, M. Sierka, E. Tapavicza, D. P. Tew, C. Van Wüllen, V. K. Voora, F. Weigend, A. Wodyński and J. M. Yu, *J. Chem. Phys.*, 2020, **152**, 184107.
93 T. Lu and F. Chen, *J. Comput. Chem.*, 2012, **33**, 580–592.
94 W. Humphrey, A. Dalke and K. Schulten, *J. Mol. Graphics*, 1996, **14**, 33–38.
95 C. Williams and T. Kelley, **http://http//www.gnuplot.info**.
96 B. Qiu, J. Wang, Z. Li, X. Wang and X. Li, *Polymers*, 2020, **12**, 310.
97 Y. Zhou, C. Ding, X. Qian and X. An, *Carbohydr. Polym.*, 2015, **115**, 670–676.
98 M. O. Ansari, M. M. Khan, S. A. Ansari, I. Amal, J. Lee and M. H. Cho, *Chem. Eng. J.*, 2014, **242**, 155–161.
99 D. Li, M. B. Müller, S. Gilje, R. B. Kaner and G. G. Wallace, *Nat. Nanotechnol.*, 2008, **3**, 101–105.
100 S. Bhattacharya, A. Ghorai, S. Raval, M. Karmakar, A. Midya, S. K. Ray and P. K. Datta, *Carbon*, 2018, **134**, 80–91.
101 J. Abd Razak, H. Hasib, N. A. Khalid, N. Mohamad, M. A. Mahamood, M. S. Mohd Suan and M. M. Ismail, *Influence of Graphene Nanoplatelets Loading into Physical and Morphological Characteristics of Polyaniline Nanocomposites*, Springer, Singapore, 2021, vol. 1.
102 Y. C. Lin, F. H. Hsu and T. M. Wu, *Synth. Met.*, 2013, **184**, 29–34.
103 Y. Lu, Y. Song and F. Wang, *Mater. Chem. Phys.*, 2013, **138**, 238–244.
104 D. Geethalakshmi, N. Muthukumarasamy and R. Balasundaraprabhu, *Optik*, 2014, **125**, 1307–1310.
105 R. B. Choudhary and A. Verma, *Opt. Mater.*, 2019, **96**, 109310.
106 R. Kandulna, R. B. Choudhary and R. Singh, *J. Inorg. Organomet. Polym. Mater.*, 2019, **29**, 730–744.
107 S. Konwer, *J. Mater. Sci.: Mater. Electron.*, 2016, **27**, 4139–4146.
108 R. B. Choudhary and R. Kandulna, *Mater. Sci. Semicond. Process.*, 2019, **94**, 86–96.
109 N. Chaudhary, M. Khanuja and S. S. Islam, *Polymer*, 2019, **165**, 168–173.
110 S. Banerjee, S. Sarmah and A. Kumar, *J. Opt.*, 2009, **38**, 124–130.
111 W. I. Singh, S. Sinha, N. A. Devi, S. Nongthombam, S. Laha and B. P. Swain, *Arab. J. Sci. Eng.*, 2022, **47**, 925–934.
112 Q. Lai, S. Zhu, X. Luo, M. Zou and S. Huang, *AIP Adv.*, 2012, **2**, 032146.
113 F. G. Souza, L. Sirelli, R. C. Michel, B. G. Soares and M. H. Herbst, *J. Appl. Polym. Sci.*, 2006, **102**, 535–541.
114 D. Maruthamani, D. Divakar, M. Harshavardhan and M. Kumaravel, *J. Chem. Pharm. Res.*, 2016, **8**, 236–244.
115 J. Bin Wu, M. L. Lin, X. Cong, H. N. Liu and P. H. Tan, *Chem. Soc. Rev.*, 2018, **47**, 1822–1873.
116 Z. S. Wu, W. Ren, L. Gao, J. Zhao, Z. Chen, B. Liu, D. Tang, B. Yu, C. Jiang and H. M. Cheng, *ACS Nano*, 2009, **3**, 411–417.
117 M. Kim, C. Lee and J. Jang, *Adv. Funct. Mater.*, 2014, **24**, 2489–2499.
118 K. Kurniasari, A. Maulana, A. Y. Nugraheni, D. N. Jayanti, S. Mustofa, M. A. Baqiya and D. Darminto, *IOP Conference Series: Materials Science and Engineering*, IOP Publishing, 2017, vol. 196, p. 12021.
119 H. Wang, Q. Hao, X. Yang, L. Lu and X. Wang, *Nanoscale*, 2010, **2**, 2164–2170.
120 G. Louarn, M. Lapkowski, S. Quillard, A. Pron, J. P. Buisson and S. Lefrant, *J. Phys. Chem.*, 1996, **100**, 6998–7006.
121 G. Niaura, R. Mažeikiene and A. Malinauskas, *Synth. Met.*, 2004, **145**, 105–112.
122 R. R. Salunkhe, S. H. Hsu, K. C. W. Wu and Y. Yamauchi, *ChemSusChem*, 2014, **7**, 1551–1556.
123 M. Jain and S. Annapoorni, *Synth. Met.*, 2010, **160**, 1727–1732.
124 J. E. Pereira Da Silva, D. L. A. De Faria, S. I. Córdoba De Torresi and M. L. A. Temperini, *Macromolecules*, 2000, **33**, 3077–3083.
125 V. Kumar, R. K. Gupta, R. K. Gundampati, D. K. Singh, S. Mohan, S. H. Hasan and M. Malviya, *RSC Adv.*, 2018, **8**, 619–631.

© 2024 The Author(s). Published by the Royal Society of Chemistry

Open Access Article. Published on 22 August 2024. Downloaded on 7/19/2025 1:42:39 AM. This article is licensed under a Creative Commons Attribution-NonCommercial 3.0 Unported Licence.

126 A. Mostafaei and A. Zolriasatein, *Prog. Nat. Sci. Mater. Int.*, 2012, **22**, 273–280.
127 R. Jain, A. Sinha, N. Kumari and A. L. Khan, *Anal. Methods*, 2016, **8**, 3034–3045.
128 S. M. Imran, Y. Kim, G. N. Shao, M. Hussain, Y. H. Choa and H. T. Kim, *J. Mater. Sci.*, 2014, **49**, 1328–1335.
129 L. Wang, Y. Ye, X. Lu, Z. Wen, Z. Li, H. Hou and Y. Song, *Sci. Rep.*, 2013, **3**, 5019–5026.
130 N. Gospodinova, L. Terlemezyan, P. Mokreva and K. Kossev, *Polymer*, 1993, **34**, 2434–2437.
131 L. Vinet and A. Zhedanov, *A 'missing' family of classical orthogonal polynomials*, Springer Science & Business Media, 2011, vol. 44.
132 J. Yan, T. Wei, Z. Fan, W. Qian, M. Zhang, X. Shen and F. Wei, *J. Power Sources*, 2010, **195**, 3041–3045.
133 A. Moyseowicz and G. Gryglewicz, *Composites, Part B*, 2019, **159**, 4–12.
134 Y. Yu, A. Xu, Y. Zhang, Z. Zhao, S. Ye and Y. Qin, *Electrochim. Acta*, 2023, **454**, 1–9.
135 Y. Li, Z. Xia, Q. Gong, X. Liu, Y. Yang, C. Chen and C. Qian, *Nanomaterials*, 2020, **10**, 1–18.
136 C. Vallés, P. Jiménez, E. Muñoz, A. M. Benito and W. K. Maser, *J. Phys. Chem. C*, 2011, **115**, 10468–10474.
137 L. Q. Xu, Y. L. Liu, K. G. Neoh, E. T. Kang and G. D. Fu, *Macromol. Rapid Commun.*, 2011, **32**, 684–688.
138 Y. Zou, Z. Zhang, W. Zhong and W. Yang, *J. Mater. Chem. A*, 2018, **6**, 9245–9256.
139 A. Fujimoto, Y. Yamada, M. Koinuma and S. Sato, *Anal. Chem.*, 2016, **88**, 6110–6114.
140 M. Shabani-Nooshabadi and F. Zahedi, *Electrochim. Acta*, 2017, **245**, 575–586.
141 F. Balqis, B. Prakoso, N. Hanif Hawari, C. Eldona and A. Sumboja, *ChemNanoMat*, 2022, **8**, e202200151.
142 V. A. Veloso, D. L. Silva, P. L. Gastelois, C. A. Furtado and A. P. Santos, *Mater. Chem. Phys.*, 2022, **285**, 126162.
143 G. G. Gebreegziabher, A. S. Asemahegne, D. W. Ayele, M. Dhakshnamoorthy and A. Kumar, *Mater. Today Chem.*, 2019, **12**, 233–239.
144 J. Park, X. Yang, D. Wickramasinghe, M. Sundhoro, N. Orbey, K. F. Chow and M. Yan, *RSC Adv.*, 2020, **10**, 26486–26493.
145 M. Li, W. Yin, X. Han and X. Chang, *J. Solid State Electrochem.*, 2016, **20**, 1941–1948.
146 Y. Li and Y. Zheng, *J. Appl. Polym. Sci.*, 2018, **135**, 1–8.
147 B. Gupta, N. Kumar, K. Panda, A. A. Melvin, S. Joshi and S. Dash, *Adv. Mater. Interfaces*, 2016, **3**, 1600161.
148 W. Y. Ching and P. Rulis, *Electronic Structure Methods for Complex Materials: The orthogonalized linear combination of atomic orbitals*, OUP Oxford, 2012, vol. 9780199575800.
149 F. E. Harris, *Adv. Quantum Chem.*, 1967, **3**, 61–127.
150 T. Clark, R. Koch, T. Clark and R. Koch, *Chem. Electron. B. Orbitals*, 1999, 5–22.
151 H. Bock, *Angew. Chem., Int. Ed. Engl.*, 1977, **16**, 613–637.
152 D. C. Fredrickson, *Bond through Code*, 2020, 55–76.
153 C. Boulechfar, H. Ferkous, A. Delimi, M. Berredjem, A. Kahlouche, A. Madaci, S. Djellali, S. Boufas, A. Djedouani, A. Errachid, A. Ali Khan, A. Boublia, T. Lemaoui and Y. Benguerba, *J. Mol. Liq.*, 2023, **378**, 121637.
154 O. Moumeni, M. Mehri, R. Kerkour, A. Boublia, F. Mihoub, K. Rebai, A. A. Khan, A. Erto, A. S. Darwish, T. Lemaoui, N. Chafai and Y. Benguerba, *J. Taiwan Inst. Chem. Eng.*, 2023, **147**, 104918.
155 A. Boublia, N. Elboughdiri, J. Georgin, K. K. Yadav, D. Ghernaout, D. S. P. Franco, M. Benaissa, A. A. M. Salih, M. Albrahim, M. S. Hamdy and Y. Benguerba, *Process Saf. Environ. Prot.*, 2024, **188**, 385–397.
156 N. Elboughdiri, H. Ferkous, K. Rouibah, A. Boublia, A. Delimi, K. K. Yadav, A. Erto, D. Ghernaout, A. A. M. Salih, M. Benaissa and Y. Benguerba, *Int. J. Mol. Sci.*, 2024, 25.
157 N. Elboughdiri, I. Lakikza, A. Boublia, S. I. Aouni, N. El Houda Hammoudi, J. Georgin, D. S. P. Franco, H. Ferkous, D. Ghernaout and Y. Benguerba, *Process Saf. Environ. Prot.*, 2024, **186**, 995–1010.
158 A. Neni, A. Boublia, M. Bouras, K. Bentoumi, M. Albrahim, N. Elboughdiri and Y. Benguerba, *J. Mol. Liq.*, 2024, **407**, 125272.
159 N. Mouats, S. Djellali, H. Ferkous, A. Sedik, A. Delimi, A. Boublia, K. O. Rachedi, M. Berredjem, A. Çukurovali, M. Alam, B. Ernsti and Y. Benguerba, *ACS Omega*, 2024, **9**, 27945–27962.
160 H. Ferkous, A. Sedik, A. Delimi, R. Redjemia, K. Abdesalem, C. Boulechfar, A. Abdennouri, A. Madaci, M. Berredjem, A. Boublia, M. Sajid Ali, B. H. Jeon, K. Kumar Yadav and Y. Benguerba, *J. Mol. Liq.*, 2024, **394**, 123781.
161 A. E. Zemouri, E. Bentouhami, H. Zaghouane-Boudiaf, Y. I. Touahria, G. Bellil, A. Boublia, N. Daas, T. Dintzer, N. Chafai, M. Albrahim, N. Elboughdiri and Y. Benguerba, *J. Environ. Chem. Eng.*, 2024, **12**, 113000.
162 T. Lemaoui, A. S. Darwish, G. Almustafa, A. Boublia, P. R. Sarika, N. A. Jabbar, T. Ibrahim, P. Nancarrow, K. K. Yadav, A. M. Fallatah, M. Abbas, J. S. Algethami, Y. Benguerba, B. H. Jeon, F. Banat and I. M. AlNashef, *Energy Storage Mater.*, 2023, **59**, 102795.
163 K. Paduszyński, *J. Phys. Chem. B*, 2018, **122**, 4016–4028.
164 A. Boublia, T. Lemaoui, G. Almustafa, A. S. Darwish, Y. Benguerba, F. Banat and I. M. AlNashef, *ACS Omega*, 2023, **8**, 13177–13191.
165 A. Szabo and N. L. Ostlund, *Modern Quantum Chemistry: Introduction to Advanced Electronic Structure Theory*, Courier Corporation, 1996.
166 J. Kahlen, K. Masuch and K. Leonhard, *Green Chem.*, 2010, **12**, 2172–2181.
167 E. Słupek, P. Makoś-Chełstowska and J. Gębicki, *Materials*, 2021, **14**, 1–20.
168 M. S. Man, M. A. M. Abdullah, S. B. Abdullah and Z. Yaacob, *Indian J. Sci. Technol.*, 2017, **10**, 1–6.
169 J. J. Prías Barragán, K. Gross, J. Darío Perea, N. Killilea, W. Heiss, C. J. Brabec, H. A. Calderón and P. Prieto, *ChemistrySelect*, 2020, **5**, 11737–11744.
170 L. Aroui, S. Madani, I. Bousnoubra, A. Boublia, I. Lakikza, S. I. Aouni, L. Abdelouahed, E. Ernst, M. Alam and Y. Benguerba, *J. Mol. Liq.*, 2024, 125818.

© 2024 The Author(s). Published by the Royal Society of Chemistry

Open Access Article. Published on 22 August 2024. Downloaded on 7/19/2025 1:42:39 AM.
This article is licensed under a Creative Commons Attribution-NonCommercial 3.0 Unported Licence.

171 C. Boulechfar, H. Ferkous, A. Delimi, A. Djedouani, A. Kahlouche, A. Boublia, A. S. Darwish, T. Lemaoui, R. Verma and Y. Benguerba, *Inorg. Chem. Commun.*, 2023, **150**, 110451.
172 Q. H. Zhang, B. S. Hou, Y. Y. Li, Y. Lei, X. Wang, H. F. Liu and G. A. Zhang, *Corros. Sci.*, 2021, **189**, 109596.
173 M. Murmu, N. C. Murmu, M. Ghosh and P. Banerjee, *J. Adhes. Sci. Technol.*, 2022, **36**, 2732–2760.
174 K. Rouibah, H. Ferkous, M. Abdessalam-Hassan, B. L. Mossab, A. Boublia, C. Pierlot, A. Abdennouri, I. Avramova, M. Alam, Y. Benguerba and A. Erto, *Molecules*, 2024, 29.
175 O. C. Adekoya, G. J. Adekoya, R. E. Sadiku, Y. Hamam and S. S. Ray, *ACS Omega*, 2022, **7**, 33808–33820.
176 M. Gabsi, H. Ferkous, A. Delimi, A. Boublia, C. Boulechfar, A. Kahlouche, A. S. Darwish, T. Lemaoui and Y. Benguerba, *Environ. Sci. Pollut. Res.*, 2023, **30**, 59081–59105.
177 F. Fuster and S. J. Grabowski, *J. Phys. Chem. A*, 2011, **115**, 10078–10086.
178 P. L. A. Popelier, *Wiley Blackwell*, 2014, 6, 9783527333, 271–308.
179 S. Garg and N. Goel, *J. Mol. Graph. Model.*, 2023, **124**, 108566.
180 T. Yasmin, A. Mahmood, M. Farooq, R. M. Sarfraz, A. Boublia, U. Rehman, M. U. Ashraf, J. K. Bhutto, B. Ernst, M. Albrahim, N. Elboughdiri, K. K. Yadav, M. A. Alreshidi, H. Ijaz and Y. Benguerba, *Int. J. Biol. Macromol.*, 2024, **268**, 131832.
181 T. Yasmin, A. Mahmood, R. M. Sarfraz, U. Rehman, A. Boublia, A. M. Alkahtani, G. S. Albakri, H. Ijaz, S. Ahmed, B. Harron, M. Albrahim, N. Elboughdiri, K. K. Yadav and Y. Benguerba, *Int. J. Biol. Macromol.*, 2024, 133468.
182 N. Sattar, H. Sajid, S. Tabassum, K. Ayub, T. Mahmood and M. A. Gilani, *Sci. Total Environ*, 2022, **824**, 153858.

© 2024 The Author(s). Published by the Royal Society of Chemistry